

Alkali-activation of marble sludge: Influence of curing conditions and waste glass addition

Original

Alkali-activation of marble sludge: Influence of curing conditions and waste glass addition / Coppola, B.; Palmero, P.; Montanaro, L.; Tulliani, J. M.. - In: JOURNAL OF THE EUROPEAN CERAMIC SOCIETY. - ISSN 0955-2219. - ELETTRONICO. - 40:11(2020), pp. 3776-3787. [10.1016/j.jeurceramsoc.2019.11.068]

Availability:

This version is available at: 11583/2836297 since: 2020-06-17T12:38:40Z

Publisher:

Elsevier

Published

DOI:10.1016/j.jeurceramsoc.2019.11.068

Terms of use:

This article is made available under terms and conditions as specified in the corresponding bibliographic description in the repository

Publisher copyright

Elsevier postprint/Author's Accepted Manuscript

© 2020. This manuscript version is made available under the CC-BY-NC-ND 4.0 license
<http://creativecommons.org/licenses/by-nc-nd/4.0/>. The final authenticated version is available online at:
<http://dx.doi.org/10.1016/j.jeurceramsoc.2019.11.068>

(Article begins on next page)

Alkali-activation of marble sludge: influence of curing conditions and waste glass addition

Bartolomeo Coppola, Paola Palmero, Laura Montanaro, Jean-Marc Tulliani

Politecnico di Torino, Department of Applied Science and Technology, INSTM R.U. Lince
Laboratory, Corso Duca Degli Abruzzi, 24, Italy

Abstract

The use of marble sludge as precursor for new alkali activated materials was assessed studying three different curing conditions (air, humid and water immersion, respectively), after an initial curing at 60 °C for 24 h, and two glass powder fractions additions (2.5 and 5.0 vol%). Microstructural, physical (drying shrinkage, Fourier transform-infrared (FT-IR) spectroscopy, X-ray spectroscopy (XPS)), thermal (differential thermal analysis – thermogravimetric analysis, DTA-TGA) and mechanical (flexural and compressive strength) properties were investigated. Air curing was the most favourable atmosphere for mechanical properties development because it promotes Si-O-Si polymerization and gel densification, as demonstrated by FT-IR and FE-SEM observations, respectively. Satisfactory mechanical properties were achieved (18 MPa and 45 MPa, for flexural and compressive strength, respectively) in particular for glass containing mixtures. Moreover, glass powder addition significantly reduced drying shrinkage of air-cured samples because it operated as a rigid aggregate in the matrix and strengthened the formed gel.

Keywords

Marble sludge; calcium carbonate; alkali-activation; waste glass; curing.

1. Introduction

The energy and environmental impact generated by quarrying companies is a major concern. Several studies highlighted that the main issues during ornamental stone processing (i.e. extraction, transportation, installation and disposal) are those related to energy, water consumption and waste management [1-5]. Waste deriving from stone industry can be divided into two categories: solid waste and stone slurry (or quarry mud). The first category includes the discarded stones or the processing wastes; the second one includes liquid or semi-liquid substances generated during sawing and polishing processes. Muds water content is reduced through filter-pressing or evaporated during slurry stocking in ponds. Depending on the type of process involved, the sludge generated is estimated over 30% of the volume of the sawn block [6]. Today, this waste is almost completely landfilled, causing the progressive but inevitable filling of the dumps. If dispersed in the air, such fine particles are harmful to human and animals, as they can induce asthma, silicosis and lung cancer [7]. Therefore, the utilization of such waste in the construction industry could be a smart solution to avoid landfilling and dust propagation in the environment. Galetakis and Soultana [8] reviewed the utilisation of quarry fines in the production of building materials. Authors found that slurries could be used as fine aggregates or as cement replacement [6,9,10] while solid wastes could partially replace aggregates in concrete mixtures [11], as already proposed in literature also for other wastes [12-16]. More eco-sustainable solutions (reuse water, use natural fibres, avoid calcination etc.) should be found to reduce the overall construction sector environmental impact [17-20]. Indeed, cement production significantly contributes to CO₂ global emissions, thus leading the research to find green alternatives to ordinary Portland cement (OPC). Among possible solutions, alkali-activated materials (AAMs) are emerging as potential alternative binders to OPC, due to superior durability and lower environmental impact [21,22]. AAMs are traditionally obtained by reaction of an alkali metal source (generally sodium or potassium hydroxide and sodium silicate) with amorphous or semi-amorphous calcium-aluminosilicate precursors [22], such as metakaolin, pozzolans, fly ashes and ground-granulated blast-furnace slag [20-25]. Very recently, some attempts to develop alkali activated materials from crystalline precursors [12,13], including marble and granite sludge [26-31], have been performed. Marble is a metamorphic rock mainly constituted of calcium carbonate (CaCO₃) while granite is a felsic intrusive igneous rock consisting of quartz, mica and feldspar (SiO₂-Al₂O₃-K₂O-Na₂O). The exploitation of granite waste in the alkaline activation process has been the

subject of different researches [26-28], including one of the authors' previous work, in which both structural dense samples and foamed materials were developed [26]. On the other side, only few studies investigated the alkali-activation of carbonates, and no previous work, at the best of our knowledge, specifically refers to the alkali-activation of marble muds. Tekin [29] developed geopolymers starting from a mixture of marble, travertine and natural pozzolan, under different curing conditions. The author achieved high compressive strength (46 MPa) under dry curing at 20°C. On the opposite, wet curing led to efflorescence and heat curing (at 75°C) increased early strength but led to cracking phenomena. Salihoglu and Salihoglu [30] used waste marble sludge in combination with several binders: cement, fly ash, clay, gypsum and blast furnace slag to prepare geopolymer pastes. Authors found that marble addition improved mechanical properties in almost all combinations. Very recently, Ortega-Zavala et al. [31] investigated the alkali-activation of limestone as single precursor with sodium hydroxide and sodium silicate. Authors found that the developed microstructure was mainly composed of a mixture of silica gel, carbonates, C-S-H, sodium calcium silicate hydrates (N-C-S-H) and sodium silicate hydrates (N-S-H). Moreover, compressive strengths ranging from 15 to 25 MPa after 360 days were determined.

Unlike previous papers, this research aims at investigating the potential of marble sludge to undergo alkaline activation. As a further point of innovation, the influence of silica from waste glass on the development of mechanical properties will be investigated as well. In fact, it is already known that the use of a readily available silica source can improve mechanical strengths and durability properties, both in traditional cements and AAMs [32-52]. For AAMs, most of the studies focused the attention on the use of rice husk ash [32-38] and silica fume [39-47] while only few papers investigated the use of glass powder [34,48-52]. Therefore, in this work, marble sludge is submitted to alkaline activation. Different curing conditions (i.e. dry, humid and wet atmospheres) and mixture compositions (i.e. different glass powder additions) are investigated. The role of these parameters on the development of fresh and hardened samples is analysed and discussed on the basis of the results of several characterisation techniques.

2. Experimental

2.1 Materials

Alkali-activated materials were prepared using waste marble sludge and waste glass powder as raw materials. A carbonatic sludge (CS), collected from an Italian marble producer (Best One s.r.l., Carrara (MS), Tuscany, Italy) was used as main source for alkali-activated materials. As-received CS was oven-dried at 80 °C for two days prior to using. A waste glass powder (GP) was supplied by an Italian company (Tecno Recuperi S.p.A., Gerenzano, Italy), that recovers recyclable materials from urban and industrial areas. In spite most of the recovered glass is sent to the glass industry stream, a huge volume of wastes still remains. This includes the finest fraction (0-4 mm, corresponding to a volume of approximately 18,000 tons/years collected by the company) used in this work. GP was submitted to several washing steps, necessary to remove most of all the contaminants (paper, aluminium, food residues, organic compounds etc.), and then dry-milled using a laboratory Turbula mixer, to achieve a fine particle size distribution.

X-ray diffraction (XRD) patterns of the CS and GP are reported in Figure 1. CS contains mainly CaCO_3 (calcite, JCPDS card n°05-0586), while $\text{MgCa}(\text{CO}_3)_2$ (dolomite, JCPDS card n°36-0426) is present as a trace (Figure 1a). On the contrary, the XRD pattern of GP presents only a wide amorphous halo, typical of glassy amorphous phase (Figure 1b).

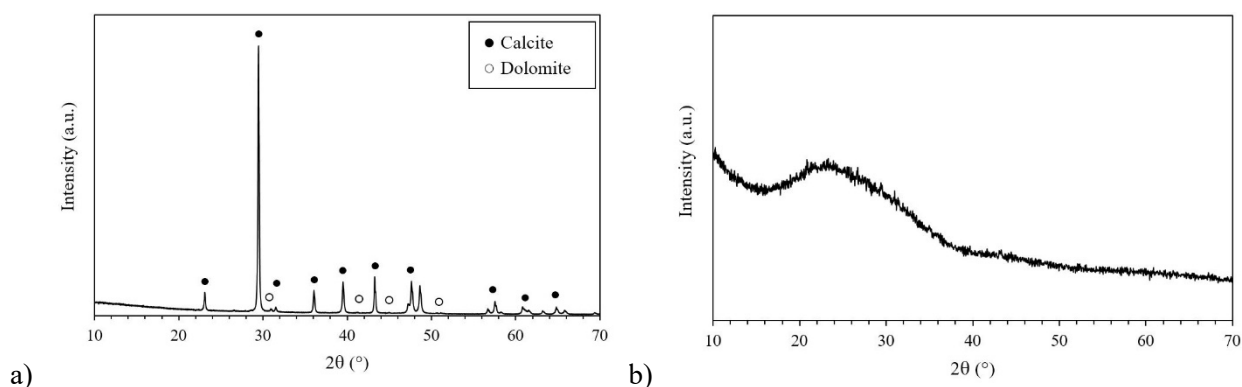


Figure 1: XRD patterns of: a) carbonatic sludge (CS); b) glass powder (GP)

Chemical composition of the starting powders was determined by X-ray fluorescence (XRF, Rigaku ZSX 100E, Tokyo, Japan) and the results are reported in Table 1. As expected, the main constituents of CS is calcium oxide, CaO , within lower amount of magnesium oxide (MgO , 1.41 wt%). XRF results are in line with

XRD analysis, confirming the presence of calcium carbonate as main constituent and dolomite as secondary phase (Figure 1). GP is mainly composed of SiO_2 (69.4 wt%), besides considering amounts of CaO and Na_2O (12.2 and 11.3 wt%, respectively), being a soda-lime glass. A limited amount of aluminium oxide is present as well (2.44 wt%), as expected in glass bottle composition.

Table 1: XRF of the carbonatic sludge (CS) and glass powder (GP)

Oxide (wt%)	CS	GP
CO_2	54.30	-
CaO	44.20	12.2
MgO	1.41	2.91
Fe_2O_3	0.07	0.51
SiO_2	-	69.4
Na_2O	-	11.3
Al_2O_3	-	2.44
K_2O	-	0.93

Particle size distribution of raw materials was determined by laser granulometry (Fritsch Analyzette 22, Idar-Oberstein, Germany) after dispersion in distilled water and sonication for 15 minutes. Frequency and cumulative frequency of the two powders are reported in Figure 2. CS particles are finer than GP ones, as evident from Table 2 which collects the particle sizes corresponding to 10% (d_{10}), 50% (d_{50}) and 90% (d_{90}) of the cumulative distribution.

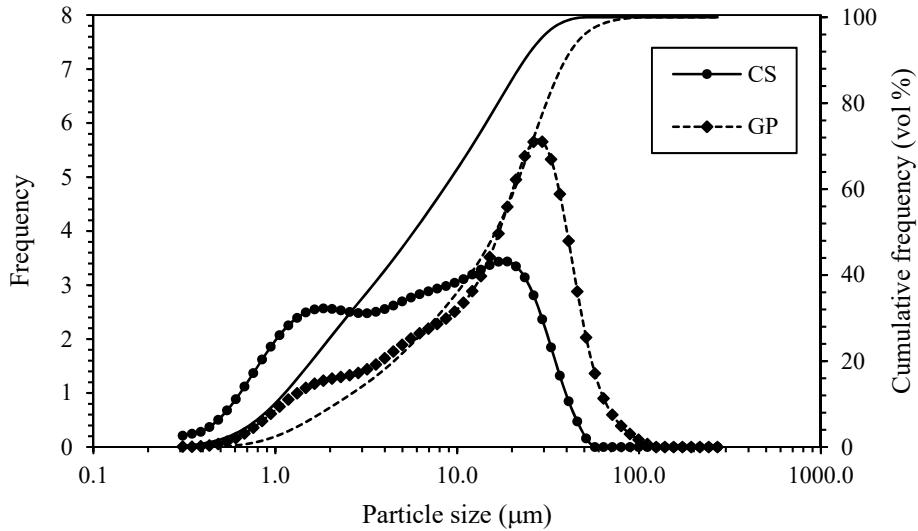


Figure 2: Particle size distribution of carbonatic sludge (CS) and glass powder (GP)

Table 2: Particle sizes at 10% (d_{10}), 50% (d_{50}) and 90% (d_{90}) of the cumulative distribution for CS and GP powders

Powder	d_{10} (μm)	d_{50} (μm)	d_{90} (μm)
CS	1.1 ± 0.1	6.1 ± 0.1	23.0 ± 1.7
GP	2.6 ± 0.3	20.2 ± 3.3	52.4 ± 11.4

FE-SEM micrographs of CS powder are reported in Figure 3a. Most of the particles have a diameter lower than $20 \mu\text{m}$, coherently to the laser granulometry distribution (Figure 2 and Table 2), in spite some larger grains are visible as well. Particles show an irregular shape with sharp edges and rough surface texture. Moreover, at higher magnifications (inset of Figure 3a), single calcite crystals can be recognized thanks to their characteristic cubic shape (ranging from few nanometers up to approximately 100 nm). These single crystals are probably due to precipitation phenomena in calcite-rich solutions when water evaporates.

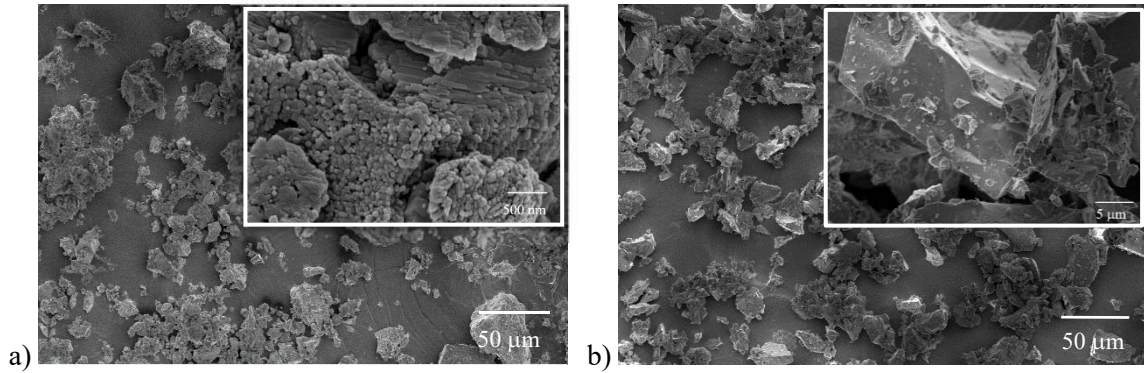


Figure 3: SEM micrographs of: a) carbonatic sludge powder (1,000 \times and 100,000 \times) and b) glass powder (1,000 \times and 10,000 \times)

Also in the case of GP (Figure 3b), particle dimensions are in line with laser granulometry. At higher magnifications (inset of Figure 3b), the irregular geometry of glass particles, the smooth surfaces typical of glasses and the conchoidal fractures due to the grinding process can be easily observed.

The alkaline solution was prepared using sodium hydroxide (NaOH pellets, Sigma-Aldrich), sodium silicate solution (containing $\text{SiO}_2 = 28.00\%$, $\text{Na}_2\text{O} = 8.28\%$ and $\text{H}_2\text{O} = 63.72\%$; pH = 11.4, density = 1.37 g/mL , Ingessil S.r.l., Montorio, Italy) and distilled water.

2.2 Samples preparation

To understand the effects of alkali-activation, curing conditions and GP addition on the developed materials, several formulations were explored.

The alkaline solution ($\text{NaOH} + \text{Na}_2\text{SiO}_3 + \text{H}_2\text{O}$) was prepared at fixed $\text{SiO}_2/\text{Na}_2\text{O}$ molar ratio (i.e. 1.65, corresponding to 14% Na_2O , 23% SiO_2 and 63% H_2O). NaOH pellets were dissolved in distilled water for 2 hours; then sodium silicate was added, and the solution was stirred for further 2 hours prior using. Pastes were prepared by mechanically mixing CS and alkaline solution for 10 minutes in a laboratory mixer (Hobart, Columbus, OH, USA). Liquid to solid volume ratio (L/S) ratio was fixed at 35/65, (considering as liquid the solution made of water, sodium hydroxide and sodium silicate) according to preliminary results. Indeed, we investigated different L/S ratios and the one used in this manuscript (i.e. 35/65) was the best one in terms of casting and compacting behaviour.

Pastes were cast into PMMA moulds to obtain prismatic samples ($2 \times 2 \times 8 \text{ cm}^3$) for mechanical tests. Alkali-activated samples were oven-cured for 24 hours at 60°C in sealed vessels before specimens demoulding. After demoulding, samples were submitted to three different curing conditions at room temperature ($20 \pm 3^\circ\text{C}$): air (relative humidity, $\text{RH} = 18 \pm 2\%$), humid ($\text{RH} = 95 \pm 2\%$) and water immersion. In particular, in the first case, specimens were exposed to laboratory RH; in the second case, specimens were sealed in a closed container with a water beaker to guarantee a constant RH; in the last one, samples were completely immersed in water. Finally, the addition of GP was investigated considering two different volume fractions (2.5 and 5.0%, respect to the volume of CS). For the formulations containing GP, the required amount of glass powder was added into the alkaline solution and kept under continuous magnetic stirring for 1 day before using.

For sake of clarity, sample designations according to curing conditions and glass waste addition are listed in Table 3. For example, CS-GP_{2.5}-A is the sample made of carbonatic sludge (CS) containing 2.5 vol% of glass powder (GP) cured in air (A).

Table 3: Nomenclature, composition and curing conditions (H = humid, A = air and W = water) of the alkali-activated materials

Sample name	Glass powder (vol%) [°]	Curing
CS-GP ₀ -A	-	Air
CS-GP ₀ -H	-	Humid
CS-GP ₀ -W	-	Water
CS-GP _{2.5} -A	2.5	Air
CS-GP _{2.5} -H	2.5	Humid
CS-GP _{2.5} -W	2.5	Water
CS-GP _{5.0} -A	5.0	Air
CS-GP _{5.0} -H	5.0	Humid
CS-GP _{5.0} -W	5.0	Water

[°]relative to the volume of CS

2.3 Samples characterization

TG-DTA analysis (Netzsch, STA 409, Selb, Germany) were performed on powdered samples, up to 1000 °C, in static air (heating and cooling rate of 10 °C/min). Before the test, water immersed samples were oven dried at 60 °C until constant mass. Specimens length variation was measured daily during the 28-days curing for all the curing conditions, in order to determine shrinkage (calculated as the ratio between the length variation and the initial length, in percentage). The results are the average values of three specimens. XRD analysis was performed on powdered samples and spectra were recorded using a Pan'Analytical X'Pert Pro instrument (Pan'Analytical, Almelo, The Netherlands) with CuK α radiation (0.154056 nm) in the 2 θ range 10-70°. Mechanical properties of alkali-activated pastes were measured using an electromechanical testing system (Zwick Roell 2014, Ulm, Germany) equipped with a load cell of 50 kN. Three point bending flexural strength and compressive strength were determined on prismatic samples (2 × 2 × 8 cm³) using a load rate of 50 and 2400 N/s, respectively. Compressive strength was determined on 2 × 2 × 4 cm³, half-samples resulting from the bending tests. To this aim, the testing machine was equipped with two steel bearing blocks: one bearing block was spherically seated and the other rigidly mounted. Mechanical properties were determined after 14 and 28 days of curing and the results are the average of three measurements for flexural tests and of six measurements for compressive tests. FT-IR measurements were performed on a Nicolet iS50 Spectrometer (Thermo Fisher Scientific, Massachusetts, USA). Spectra were recorded in attenuated total reflectance (ATR) mode in the range 4000-400 cm⁻¹. X-Ray Photoelectron Spectroscopy (XPS) was carried

out with a PHI-5000 Versaprobe instrument (Physical Electronics, Chanhassen, MN, USA) using an AlK α monochromatic source. Survey scans (collected in the range 0-1200 eV) and high resolution (HR) O(1s) spectra (523-543 eV) were acquired using a 100 μ m X-rays spot. HR spectra were shifted, in the binding energy scale, in order to place the C(1s) peak at 285 eV, to compensate surface charging phenomena [53,54]. Morphologies of powders and alkali-activated pastes (both on polished and fracture surfaces) were examined by means of a FE-SEM (Zeiss Supra-40, Oberkochen, Germany) equipped with an Oxford Energy Dispersive X-ray detector. All observations were performed after sputtering samples with a thin coating of platinum.

Finally, all samples were immersed into tap water to check their durability in wet conditions.

3. Results and Discussion

3.1 Shrinkage

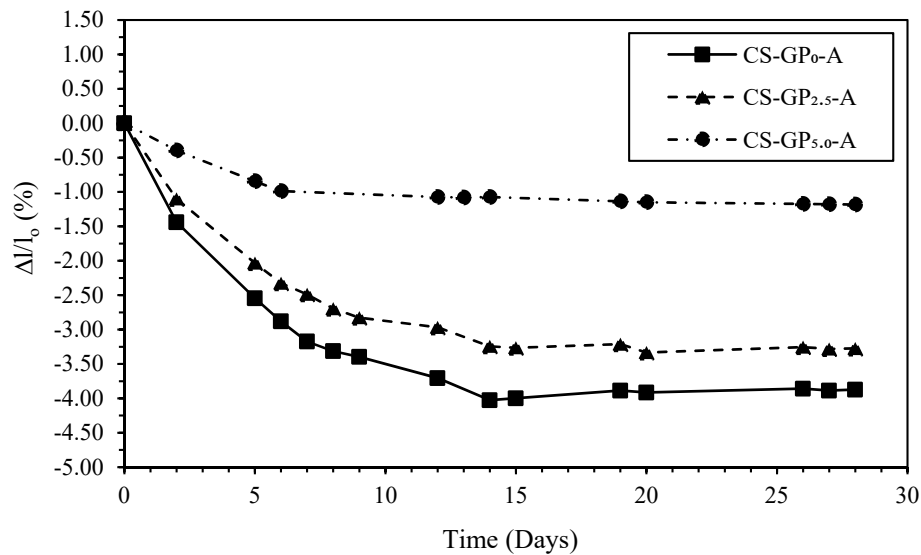
Mass and length variations were measured daily, for air, humid and water-immersed samples during the 28 days curing period. It is well known that alkali activated binders tend to exhibit relative high drying shrinkage [55,56] but information are missing concerning humid and wet curing. From Figure 4, it is clear that the three different curing conditions play a key role on specimens' shrinkage.

Air cured samples show the highest length variation (Figure 4a) compared to the other two curing conditions and, in parallel, the highest mass loss (not shown). For CS-GP₀-A and CS-GP_{2.5}-A samples, most of the shrinkage occurs during the first ten days, where the shrinkage rate is higher, while for CS-GP_{5.0}-A samples during the first five days; after that, for all the samples, a constant value was attained. At the end of the test (i.e. after 28 days), the shrinkage of glass containing samples was significantly lower respect to the reference sample (shrinkage values are - 3.87%, -3.28% and -1.18% for CS-GP₀-A, CS-GP_{2.5}-A and CS-GP_{5.0}-A, respectively). Two main explanations can be given: first, undissolved glass particles act as a rigid aggregate, contrasting shrinkage phenomena; second, the reaction products of glass-containing mixtures have an improved strength respect to glass-free formulations, in agreement with Zhang and Yue [49] who obtained similar results for alkali-activated slag mortars containing waste glass powder. Finally, for CS-GP_{5.0}-A

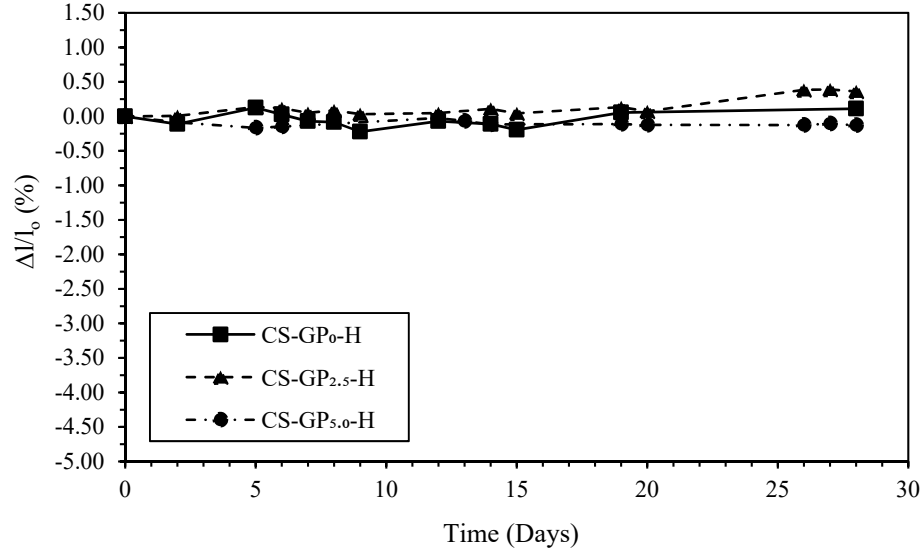
samples, thanks to the relative high glass powder content (5.0 vol%), no length variations were observed after 6 days, while for the other two mixtures meaningful length variations were recorded up to 15 days.

Considering humid-cured samples, no meaningful length (Figure 4b) and mass variations were recorded during the curing period, meaning that samples were water and/or water vapour saturated during all the curing period with no hygrometric variations (i.e. drying shrinkage).

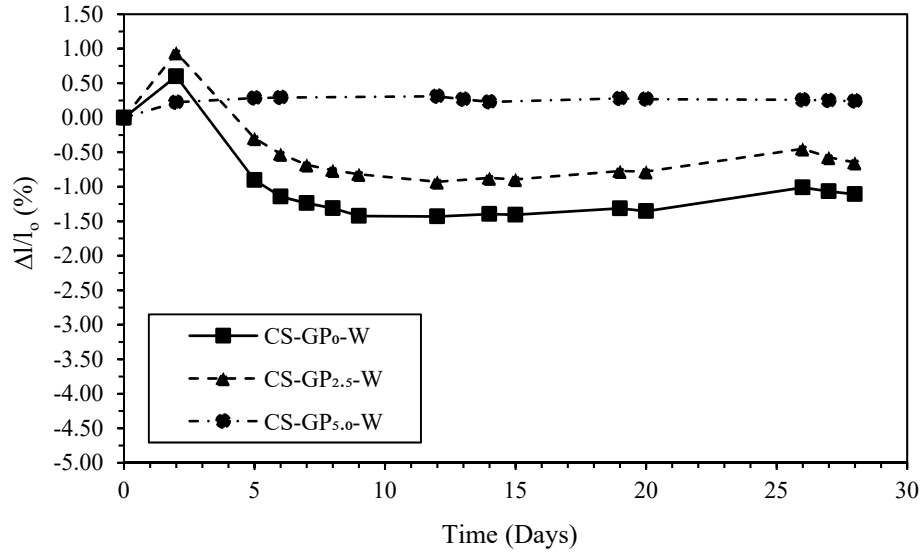
Finally, considering length variation of water immersed samples (Figure 4c), two different behaviours can be distinguished. All the samples expand during the first days of immersion, and particularly CS-GP₀-W (i.e. without glass) and CS-GP_{2.5}-W (i.e. with 2.5 vol% of glass) samples. Then, these two materials shrink up to the tenth day of immersion, while CS-GP_{5.0}-W (i.e. containing 5.0 vol% of glass) doesn't shrink after the initial light expansion. This behaviour can be explained considering that water immersed samples absorb water during the first days, i.e. mass increases (data not reported), while after few days, they start to loss mass, due to the dissolution into water of some compounds, as will be discussed later. Thus, in the initial stage, contextually to water absorption, some swelling occurs; later, after 5-7 days approximatively, samples start to shrink due to matrix dissolution. Once again, the presence of higher amounts of glass powder (i.e. 5.0 vol%) was effective in reducing shrinkage phenomena as previously discussed.



a)



b)



c)

Figure 4: Length variation of alkali-activated carbonatic sludge specimens: a) air-cured, b) humid cured and c) water immersed

Comparing length variations of air-cured specimens and considering glass content and curing time (Figure 5), two considerations can be drawn. First, higher the glass content, lesser the shrinkage; second, higher the glass content, lower the time to achieve a constant length. Hence, glass powder addition is very useful in contrasting shrinkage phenomena.

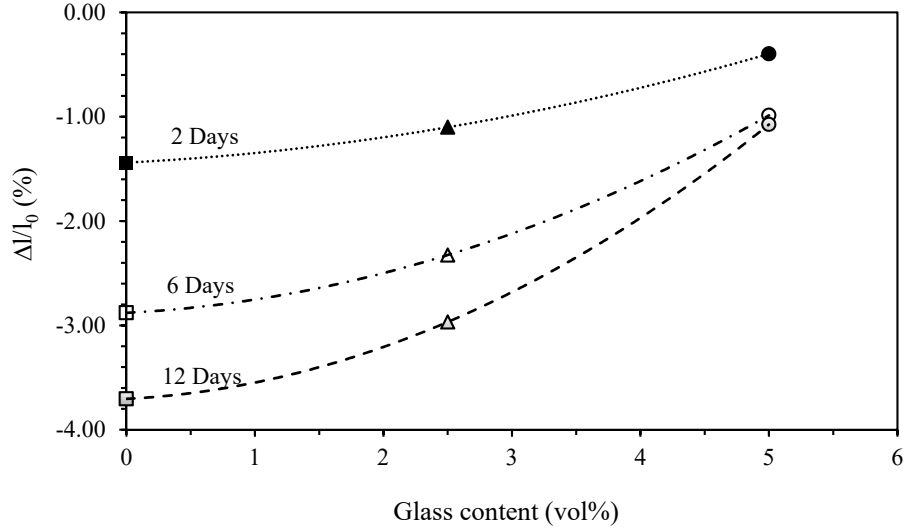


Figure 5: Length variation of the air-cured specimens after 2, 6 and 12 days for the different glass volume fractions

3.2 XRD

XRD patterns of the alkali-activated pastes after 28 days of curing in different conditions are reported in Figure 6. The sharp peaks of the phases composing the starting sludge (calcium carbonate and dolomite) are still present in the hardened samples, for all the curing environments. However, in the case of air cured specimens (CS-GP₀-A), some new peaks (inset of Figure 6) corresponding to sodium carbonate hydrate (thermonatrite, Na₂CO₃·H₂O, JCPDS card n°08-0448) were observed. On the other side, GP addition shows no influence on the formation of new crystalline phases, independently of curing conditions.

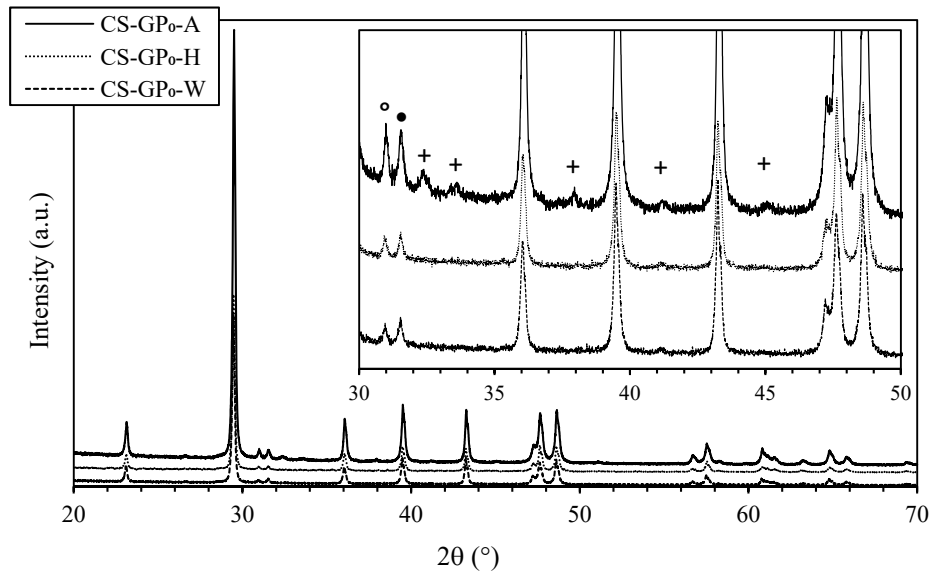


Figure 6: XRD pattern of the alkali-activated carbonatic sludge after curing in different conditions (○ = Dolomite; ● = Calcite; + = Thermonatrite)

3.3 Thermal analysis

Thermal analysis of the oven-dried carbonatic sludge is reported in Figure 7. DTA shows an endothermic peak at 930 °C corresponding to a total weight loss of 43%, as given by TGA curve. Decomposition of dolomite (in magnesium oxide, MgO, and carbon dioxide, CO₂) and calcite (in calcium oxide, CaO, and CO₂) starts at 720 °C and ends at 975 °C. As reported elsewhere [28,57], dolomite and calcite decomposition peaks are not separated when the test is carried in air atmosphere, as in the present case.

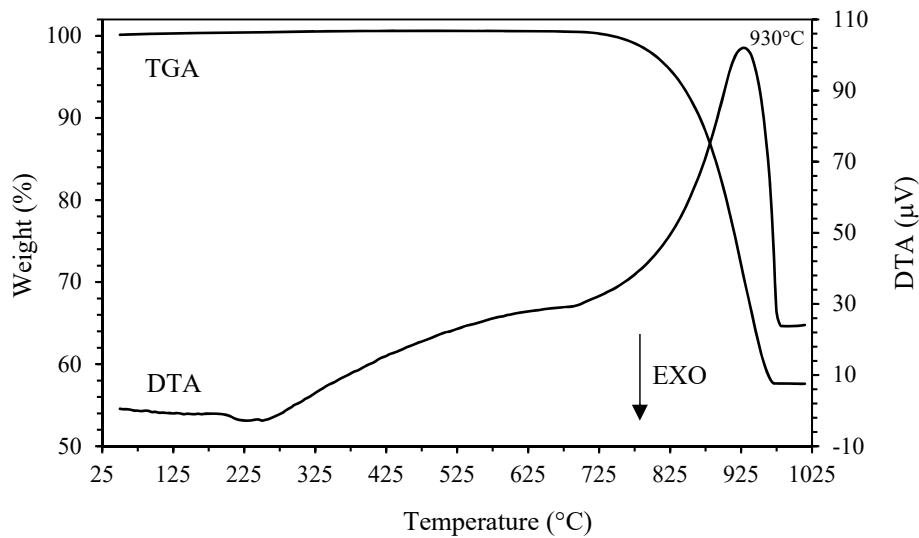


Figure 7: TGA-DTA in air of dried carbonatic sludge

Thermal analysis of the alkali-activated CS after 28 days of curing in the different environmental conditions are reported in Figure 8. TGA-DTA curves can be divided in three different zones: 50-175°C, 500-750°C and 750-1000°C. No meaningful differences were noted on samples containing or not glass powder. Thus, only TGA-DTA curves of alkali-activated CS without glass powder are here discussed.

The weight loss in the first range (50-175°C) corresponds to water evaporation and dehydration. As expected, the moisture content (free water + adsorbed water) is higher in CS-GP₀-H samples than in CS-GP₀-A specimens because the high RH of the humid environment prevented moisture evaporation. In particular, the weight loss of the samples cured in humid environment (CS-GP₀-H) corresponds to 10 wt%, while that of air cured samples (CS-GP₀-A) corresponds to only 2 wt%. In this latter case, thermonatrite dehydration also occurs at low temperature, leading to anhydrous sodium carbonate [58]. On the contrary, specimens cured

under water immersion do not display weight loss in this temperature range since they were oven dried at 60°C before the test (see sample characterization, § 2.3). For air and humid-cured samples, the different contributions related to water evaporation phenomena were separated through DTG peak deconvolution (Figure 9).

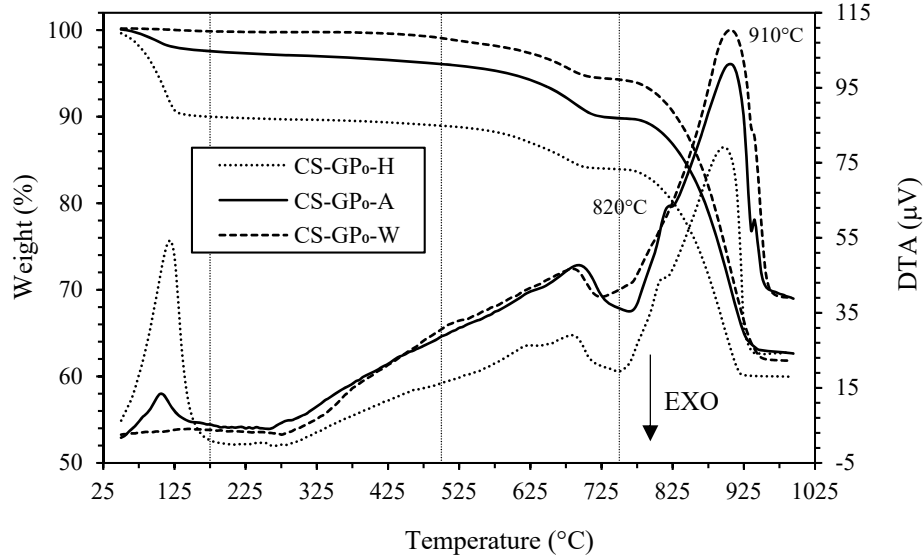


Figure 8: TGA-DTA in air of the alkali-activated carbonatic sludge after curing in different conditions

DTG curve of CS-GP₀-A sample can be deconvoluted into three contributions (Figure 9a) which correspond to *i*) evaporation of water from pores (free water), peak at 74 °C, *ii*) adsorbed water as well as dehydration of possible C-S-H species, peak at 102 °C, and *iii*) thermonatrite water molecules loss [58], peak at 136 °C, respectively. On the contrary, the DTG curve of CS-GP₀-H sample (Figure 9b) shows only two contributions, since the signal due to thermonatrite dehydration is not present. Coherently to what previously shown in the XRD section (§ 3.4) thermonatrite was formed only in air-cured materials.

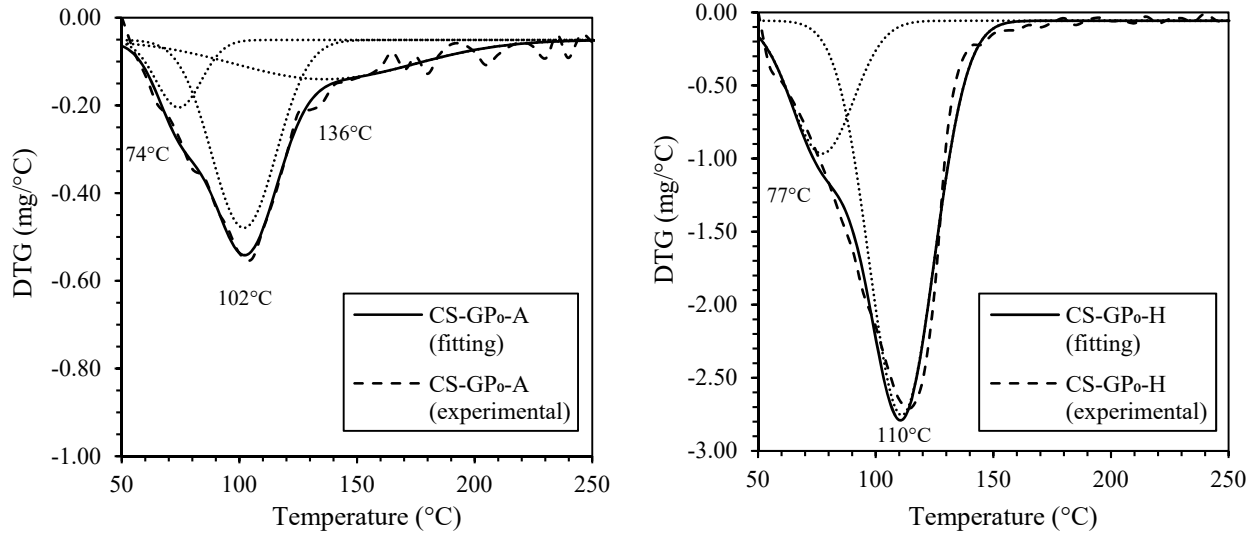
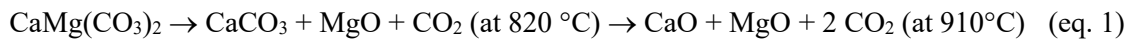


Figure 9: DTG of (a) CS-GP₀-A and (b) CS-GP₀-H in the range 50-250 °C

Weight loss in the range 500-750°C can be related to two different thermal decompositions: the first one (629-641 °C) could be due to poorly crystalline forms of CaCO₃ (aragonite, vaterite, and amorphous calcium carbonate) decomposition [59] while the second one (681-691 °C) is probably due to sodium carbonate, Na₂CO₃, decomposition. Usually, sodium carbonate melting happens above 800 °C in air [60]. However, the presence of fine silica can lower the beginning of its decomposition temperature down to 500°C [60]. Finally, the peak in the third range (750-1000°C) corresponds to calcium carbonate and dolomite decomposition with a weight loss of about 22% for water and humid cured samples and 28% for air cured samples. The shoulder at 820 °C of the DTA curves could be due to dolomite double stage thermal decomposition [61]:



3.4 FT-IR

Figure 10 depicts the FT-IR spectrum of CS powder showing the typical spectrum of calcite. The main IR bands correspond to the symmetric and asymmetric vibrations of the carbonate ion (CO_3^{2-}): 713 cm^{-1} (mode ν_4); 874 cm^{-1} (ν_2); 1130 cm^{-1} (ν_1); 1390 cm^{-1} (ν_3) and 1794 cm^{-1} (C=O groups) [53].

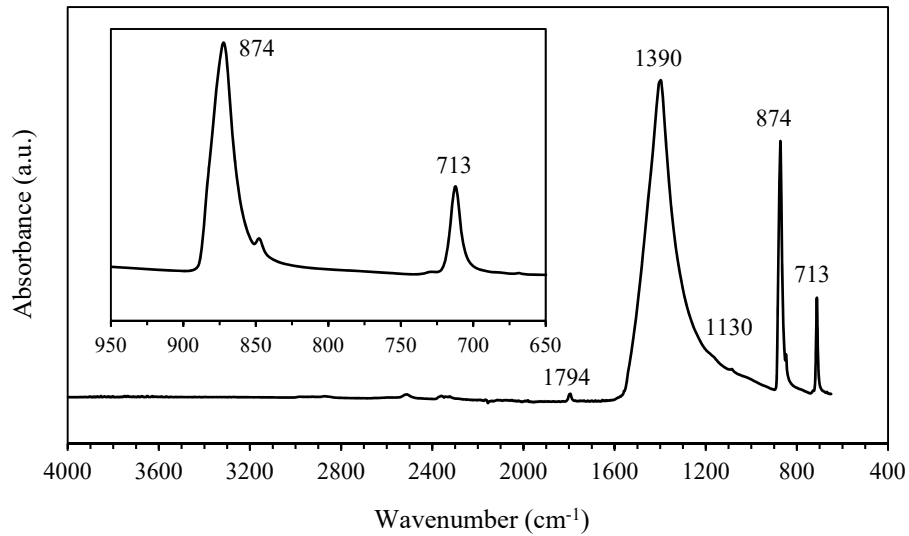


Figure 10: FT-IR of CS and detail of the $650\text{--}950\text{ cm}^{-1}$ range

FT-IR spectrum of glass powder (Figure 11) shows three main absorption bands at 962 , 769 and 450 cm^{-1} , corresponding to asymmetric stretching vibration of Si-O-Si, symmetric stretching vibration of Si-O-Si and bending vibration of O-Si-O, respectively [62].

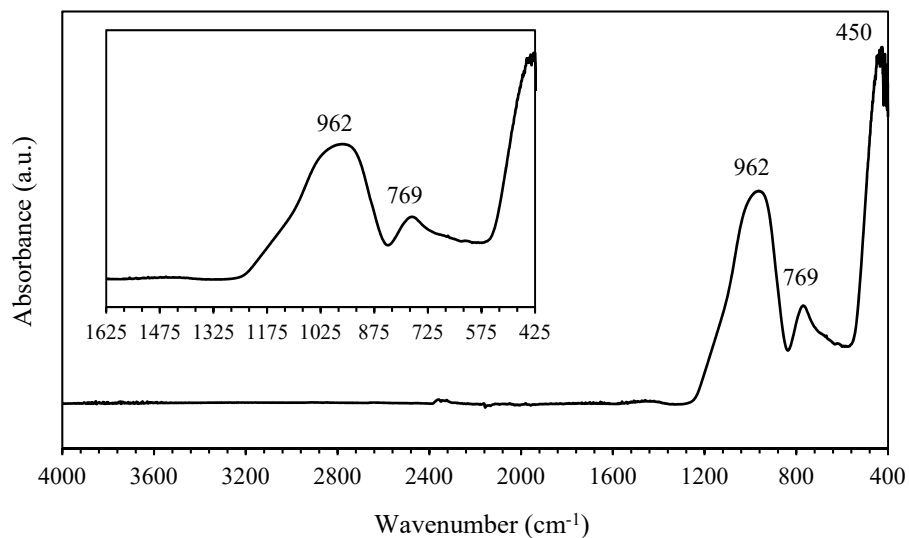


Figure 11: FT-IR of glass powder and detail of the $425\text{--}1625\text{ cm}^{-1}$ range

FT-IR of the CS-GP₀ compositions, powdered after exposure for 28 days at the different curing conditions, are reported in Figure 12. All the specimens show similar spectra containing the main peaks of calcium carbonate previously discussed but some differences in the range 450-1250 cm⁻¹ (inset of Figure 12) can be observed. The broad band in the range 800-1200 cm⁻¹ corresponds to the Si-O vibrations [63]. In particular, to better determine all the contributions, spectra deconvolution in the 900-1200 cm⁻¹ range was performed (Figure 13). Four different curves can be identified, corresponding to: *i*) asymmetric stretching vibrations in the Si-O bonds of silica tetrahedra in C-S-H in the Q² coordination status (950-970 cm⁻¹) [31,63], *ii*) bending vibrations of Si-O bonds of the silica gel (990-1020 cm⁻¹) [31] and Si-O stretching vibrations in a silicon-rich gel (*iii*) 1060-1080 cm⁻¹ and *iv*) 1125-1150 cm⁻¹) [63]. The C-S-H Si-O bonds bending vibrations band is present in all the investigated formulations (i.e. for all the curing conditions), with a higher intensity for the air-cured specimen. This can be explained considering an initial formation of C-S-H during the first day of curing at 60°C in a sealed vessel, for all samples. Then, polymerisation and condensation reactions were favoured only in the case of air cured specimens while were hindered or delayed in the other two curing environments. As demonstrated elsewhere [64,65], calcite solubility is strongly influenced by NaOH concentration: at high NaOH molarities, Ca²⁺ is converted into Ca(OH)₂ due to the large amount of available OH⁻ [64]. Moreover, the presence of silica in the activating solution promotes pozzolanic reactions resulting in the formation of (N)-C-S-H, sodium and calcium rich silica gel and carbonates. In fact, Ca²⁺ cations can react with sodium silicate to produce C-S-H thanks to the cation exchange (substitution of sodium with calcium) and sodium silicate crystallises only once that water is evaporated [66,67], as occurs under air-curing condition. Avila-López et al. [68] and Ortega-Zavala et al. [31] reported similar results attributing the formation of C-S-H to the reaction between Ca²⁺ ions and silica from waterglass. Indeed, air cured specimens show a more intense band around 950-970 cm⁻¹, representative of a higher amount of C-S-H. Considering the area of the deconvoluted components and, in particular, the ratio between the area around 1000 cm⁻¹ and 960 cm⁻¹, an increase of the ratio was obtained for air, humid and water cured samples (2.45, 3.08 and 4.90, respectively) (Figure 13). Moreover, the area of the peak around 1060-1080 cm⁻¹ is higher for humid and water cured samples than for air cured materials meaning the precipitation of a higher amount of calcium-free silica gel for humid and water curing conditions. Considering peak position, C-S-H of air cured samples has a higher degree of polymerisation because the corresponding peak is shifted toward higher wavenumbers

respect to humid and water cured samples [63,69]. A further confirmation of the higher degree of polymerisation is the presence of a peak at 670 cm^{-1} , representative of the Si-O-Si bending and a broad signal of the Si-O-Si symmetric stretching vibration appears at 785 cm^{-1} [70,71].

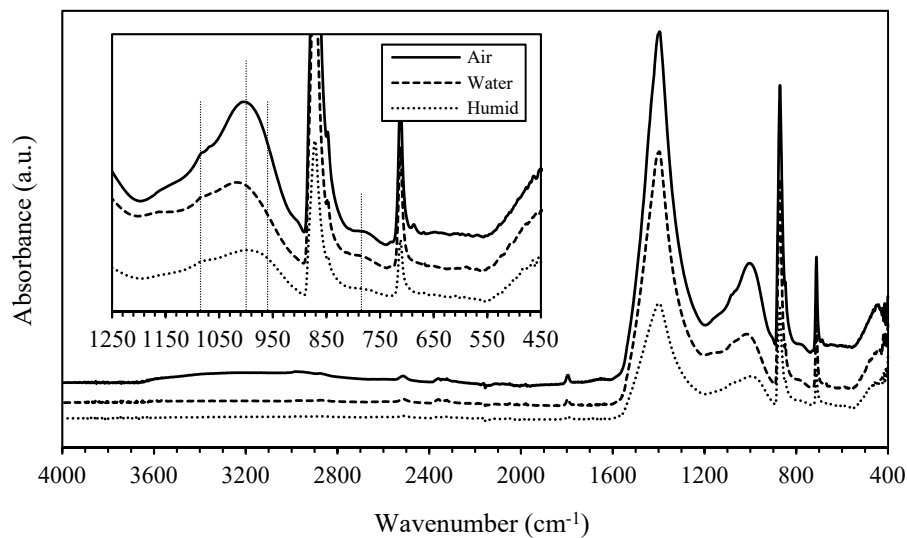


Figure 12: FT-IR of CS-GP₀ and detail of the $450\text{--}1250\text{ cm}^{-1}$ range

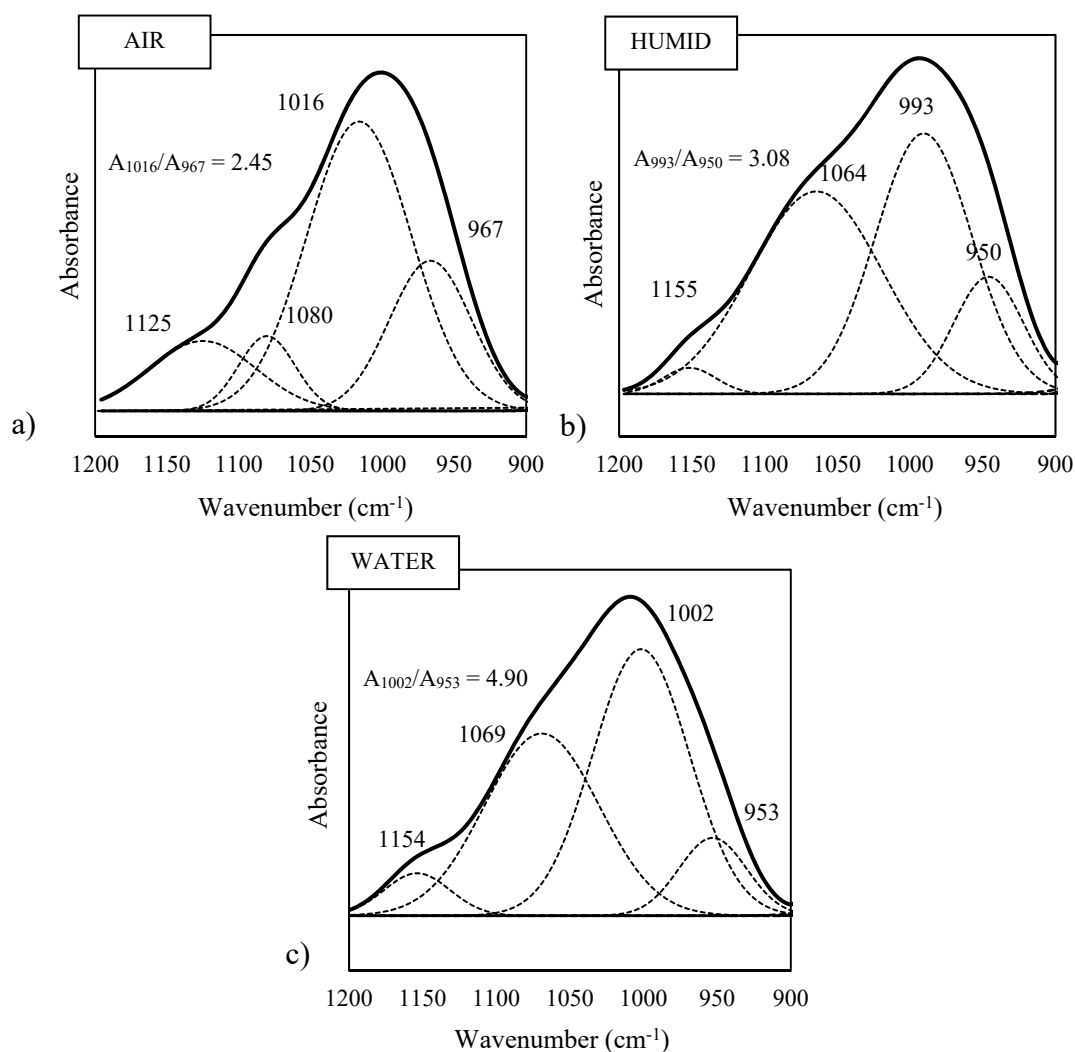


Figure 13: Deconvolution of the Si-O vibrations band for CS-GP₀ compositions exposed at different curing conditions: a) air; b) humid and c) water

FT-IR of CS-GP_{2.5} and CS-GP_{5.0} are reported in Figure 14 and Figure 15, respectively. Spectra are similar to that of CS-GP₀, the only difference is the shift toward higher wavenumbers of the peak corresponding to Si-O vibrations, representative of a further increase of the degree of polymerisation thanks to the presence of glass powder.

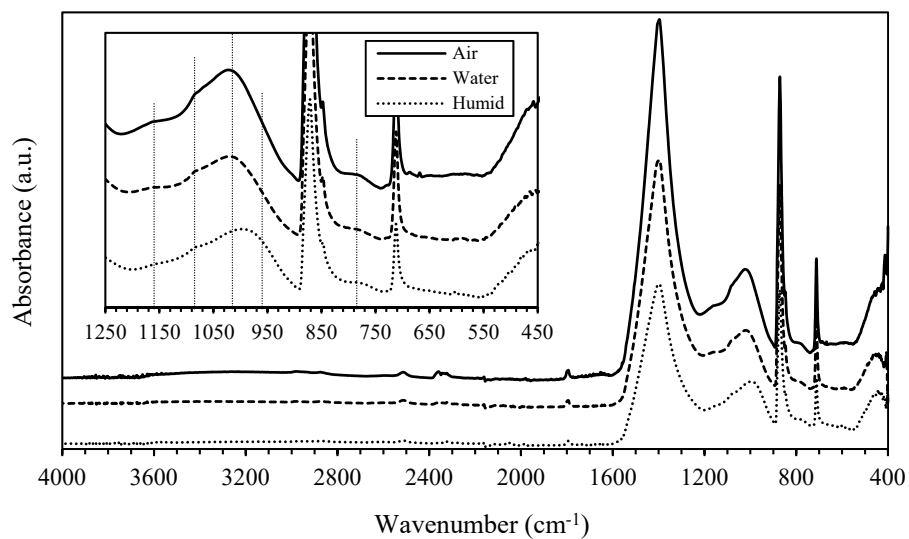


Figure 14: FT-IR of CS-GP_{2.5} and detail of the 450-1250 cm⁻¹ range

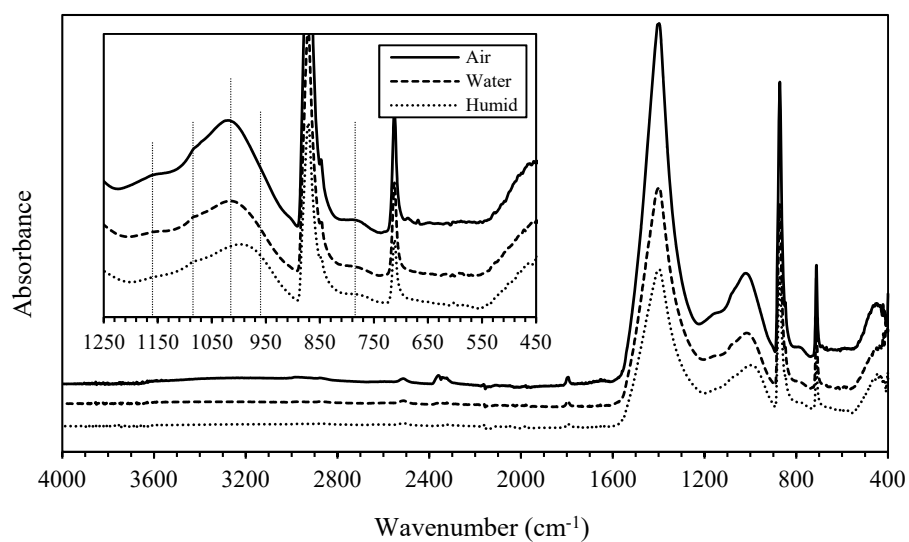


Figure 15: FT-IR of CS-GP_{5.0} and detail of the 450-1250 cm⁻¹ range

3.5 XPS

Figure 16 shows the high-resolution XPS O(1s) spectra of the starting powders, namely soda-lime glass (Figure 16a) and carbonatic sludge (Figure 16b). Soda-lime glass O(1s) spectrum presents three peaks at 530.35, 532.20 and 536.52 eV corresponding to non-bridging oxygen (NBO), bonded bridging oxygen (BO) and Na-KLL Auger peak, respectively [54,72]. Oxygen atoms of the first group (i.e. NBO) are covalently bonded to one SiO₄ tetrahedron and ionically bonded to one alkali (i.e. sodium) or alkaline earth (i.e. calcium) while BO are covalently bonded oxygen atoms that connect two SiO₄ tetrahedra. The deconvolution of CS powder XPS O(1s) spectrum shows two peaks. In particular, the first one (labelled O_I) at 531.51 eV corresponds to the oxygen atoms of the O-Ca bonds while the second one (O_{II}) at 532.69 eV is representative of the C-O oxygen atoms [53].

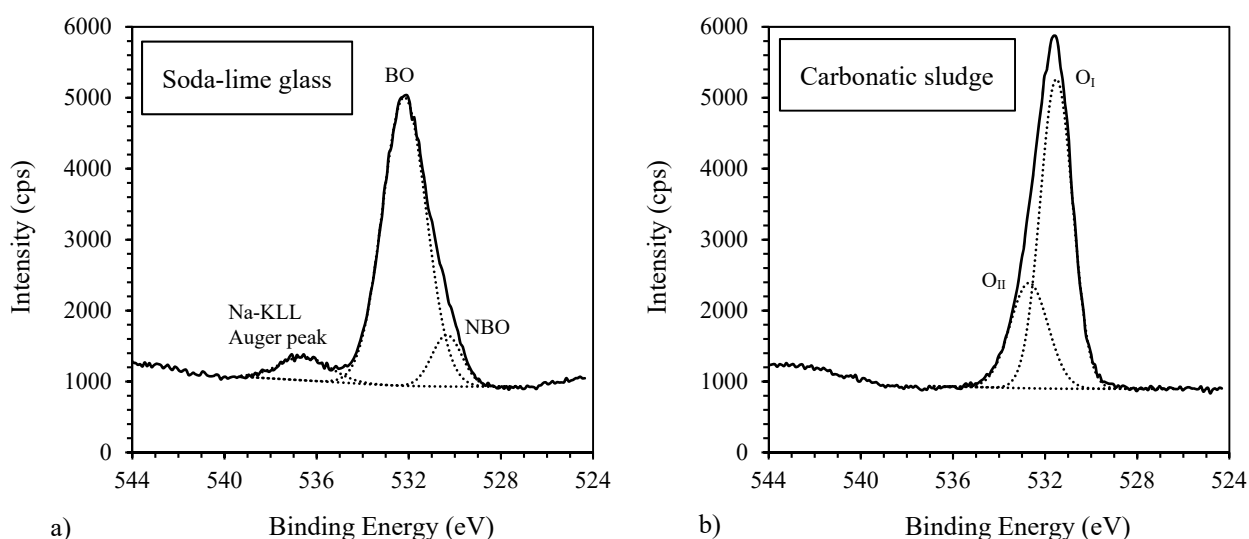


Figure 16: XPS O(1s) spectra of (a) soda-lime glass and (b) carbonatic sludge (dotted lines show the fitting results)

O(1s) spectra of CS-GP₀ mixtures cured for 28 days under the different conditions are shown in Figure 17 and several differences in spectra shape and intensity can be recognised. Spectra can be deconvoluted in four peaks moving from lower to higher binding energies, corresponding to NBO (Si-O-Ca or Si-O-Na), BO (Si-O-Si), silanol groups (Si-OH) and Na KLL Auger peak, respectively [73-75]. CS-GP₀-A spectrum (Figure 17a) has the highest intensity and the main contribution is due to NBO peak (531.33 eV) while CS-GP₀-H and CS-GP₀-W (Figure 17b and c, respectively) are shifted toward higher binding energies due to an increase of the contribution of the silanol groups located at 533.28 and 533.24 eV, respectively. Moreover, as reported by Black et al. [73,76], the difference between BO and NBO binding energies ($\Delta_{\text{BO-NBO}}$) is representative of

the degree of polymerisation: lower the difference, higher the degree of polymerisation. In our work, the lowest values of $\Delta_{\text{BO-NBO}}$ were calculated for air cured samples. These results confirm FT-IR analysis of a more condensed gel network with stronger Si-O-Ca(Na) bonds for air cured samples. O(1s) spectra of samples containing glass powder show the same trend and no meaningful variations are observed.

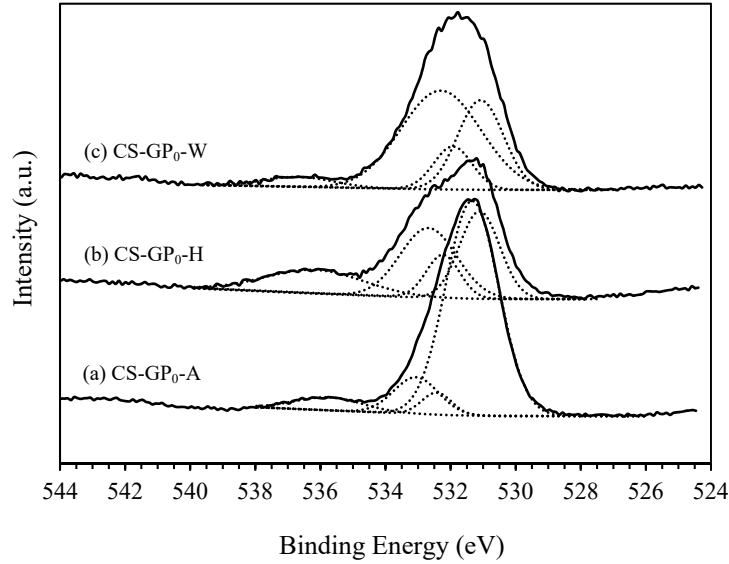


Figure 17: XPS O(1s) spectra of (a) CS-GP₀-A, (b) CS-GP₀-H and (c) CS-GP₀-W (dotted lines show the fitting results)

3.6 Mechanical properties

Flexural and compressive strength of alkali-activated CS after 14 and 28 days of curing are reported in Figure 18 and Figure 19, respectively. Air-cured samples show higher mechanical properties compared to the humid and water cured specimens. In fact, in agreement with FT-IR and XPS results, both C-S-H formation and increase of the polymerisation degree of Si-O-Si bonds lead to higher mechanical properties.

Considering flexural strength, no meaningful differences between 14 and 28 days of curing for humid and water cured samples can be observed. On the contrary, flexural strength of air-cured samples considerably increases between 14 and 28 days, particularly for glass containing samples (Figure 18). Regarding compressive strength, curing conditions also strongly influence the results. Air-cured samples always show higher compressive strength than humid and water cured samples. In addition, curing time was effective only in CS-GP₀-A, showing a certain increase in compressive strength from 14 to 28 days (Figure 19). For samples cured under humid and water conditions, no strength increase with increasing time was observed. In particular, compressive strengths at 28 days of CS-GP₀-A, CS-GP_{2.5}-A and CS-GP_{5.0}-A are 38, 42 and 45

MPa, respectively. As regard as glass powder addition, a pozzolanic activity of glass particles is supposed. Such activity depends on several parameters, and particularly on NaOH concentration and particle size [48-52,77-80]. In our study, very fine glass particles (Table 2) and high alkaline solution (pH = 12.7) are used, thus promoting glass particles dissolution. Therefore, glass addition leads to a compressive strength increase, compared to the reference sample, of 9 and 17 %, for 2.5 and 5.0 vol%, respectively. Glass addition strongly influences the compressive strength also for the other two curing conditions. In particular, after 28 days of curing, an increase of compressive strength of about 30% and 60% was measured for humid and water cured samples, respectively. Moreover, in the case of water cured samples, the strong influence of glass addition suggests an increase of the hydraulicity of the mixture, and it is also responsible of the durability improvement. As a matter of fact, glass containing mixtures well withstand after water immersion and no cracks are observed on their surface.

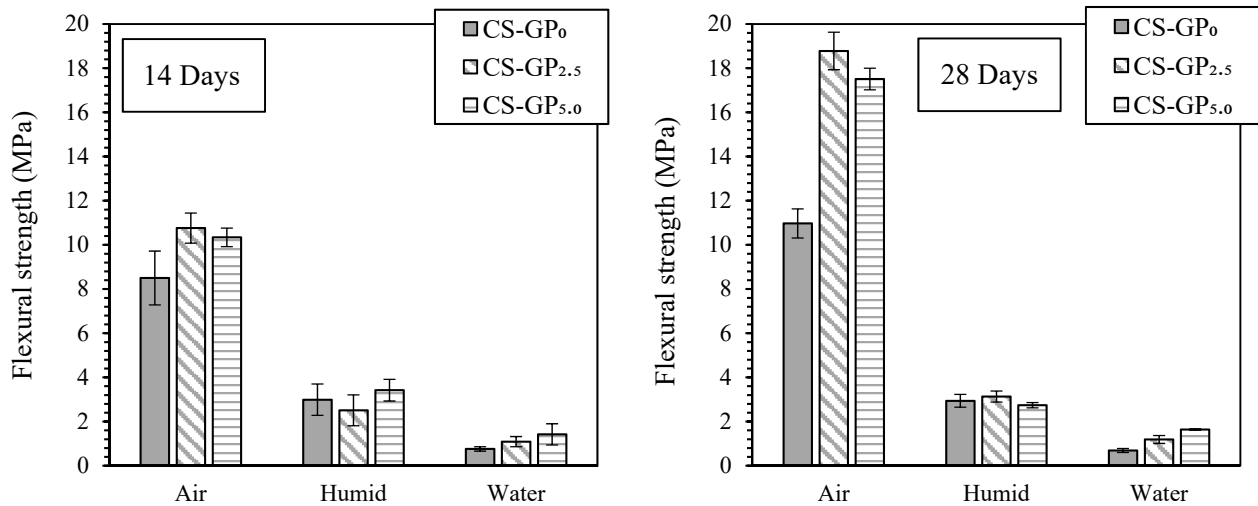


Figure 18: Flexural strength of alkali-activated carbonatic sludge after curing in different conditions for a) 14 days and b) 28 days (GP_{2.5} and GP_{5.0} means 2.5 and 5.0 vol% of glass powder)

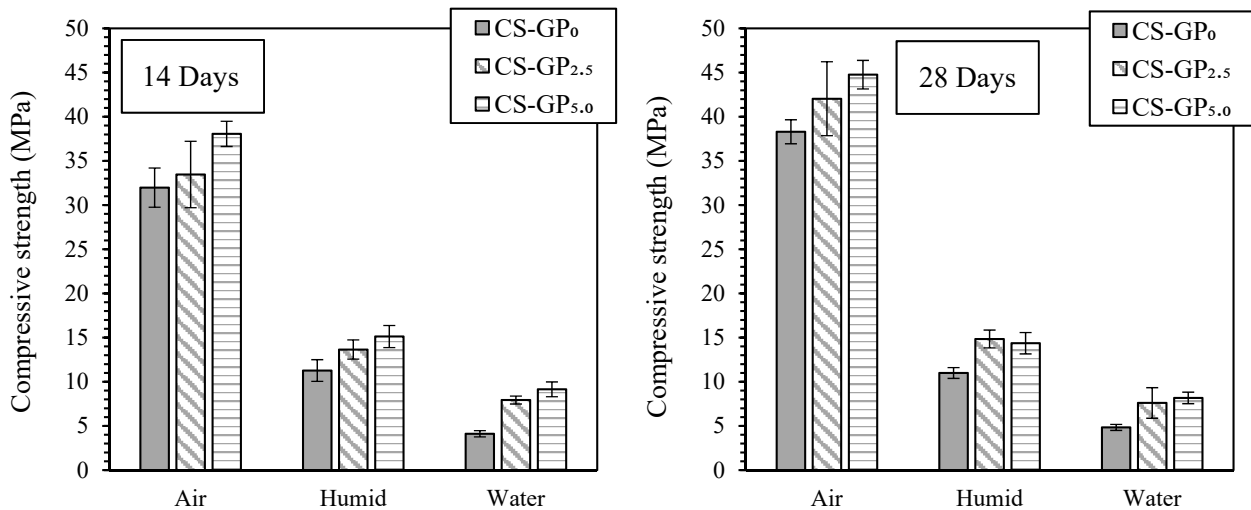


Figure 19: Compressive strength of alkali-activated carbonatic sludge after curing in different conditions for a) 14 days and b) 28 days (GP_{2.5} and GP_{5.0} means 2.5 and 5.0 vol% of glass powder)

3.7 Microstructure and EDS analysis

FE-SEM pictures of polished surfaces (magnification 1,000 ×) of alkali-activated carbonatic sludge after 28 days of curing in different conditions are reported in Figure 20. Regardless the curing environment, numerous pores due to entrapped air during samples casting and compaction are clearly visible. In the case of air and humid cured samples, bulk matrix is homogenous and highly dense. However, near the pores a less dense structure is visible probably due to the water and/or water vapour contained in the pores. Such phenomenon is more pronounced in humid cured samples (Figure 20b) than in air cured ones (Figure 20a) while in water cured samples the matrix is characterized by a diffuse microporosity (Figure 20c) due to the dissolution of some compounds in water during curing. For humid-cured samples, the high pH of the pore solution avoid the progressive polymerization of C-S-H because dissolves the forming matrix near the pores (Figure 20b and Figure 21b), leading to lower mechanical properties. Figure 21 reports the FE-SEM images of the pores content for the different curing conditions. It is clear that air cured samples present a thicker gel phase (Figure 21a) compared to the other two curing environments. These results confirm the hypothesis that air curing allows the increase of the polymerisation degree thanks to a lower relative humidity that strengthens the matrix and confers higher mechanical properties.

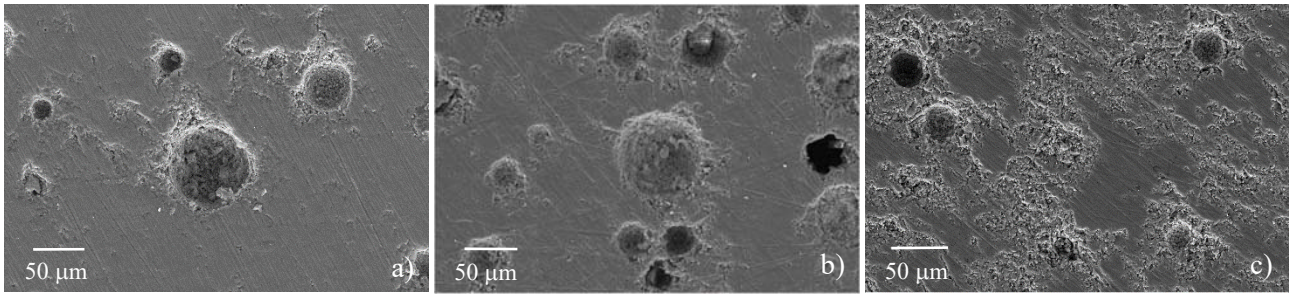


Figure 20: FE-SEM micrographs on polished surfaces (magnification 1,000 ×) of alkali-activated carbonatic sludge after curing in different conditions: a) CS-GP₀-A, b) CS-GP₀-H and c) CS-GP₀-W

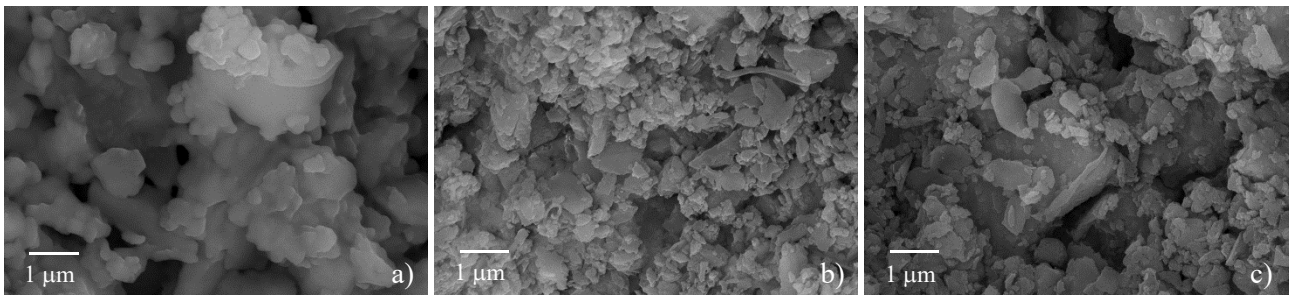


Figure 21: FE-SEM micrographs of the pores content (magnification 50,000 ×) of alkali-activated carbonatic sludge after curing in different conditions: a) CS-GP₀-A, b) CS-GP₀-H and c) CS-GP₀-W

Considering water cured samples, the formation of a white gel was observed both on samples surfaces and in the water of curing. To determine the composition of such gel, samples were oven dried at 60°C for two days before XRD analysis. The gel presents a broad amorphous halo, that could correspond to the silica dissolved in water, and some crystalline phases: trona (sodium hydrogen carbonate hydrate, $\text{Na}_3\text{H}(\text{CO}_3)_2(\text{H}_2\text{O})_2$, JCPDS card n°29-1447), sodium carbonate hydrate (thermonatrite, $\text{Na}_2\text{CO}_3 \cdot \text{H}_2\text{O}$, JCPDS card n°08-0448), sodium calcium silicate ($\text{Na}_4\text{CaSi}_3\text{O}_9$, JCPDS card n°24-1069) and calcium silicate (Ca_3SiO_5 , JCPDS card n°17-0445). The formation of such compounds is coherent to what previously discussed at the beginning of this paragraph concerning the presence of voids due to matrix removal (Figure 20c). Moreover, comparing EDS analysis of CS-GP₀-A, CS-GP₀-H and CS-GP₀-W it is evident the reduction of the atomic percentage both of silicon and sodium due to their leaching in water during curing. Indeed, Ca/Si and Si/Na atomic ratio are 7.30 and 0.73, 7.47 and 1.06, 11.90 and 2.27, for CS-GP₀-A, CS-GP₀-H and CS-GP₀-W, respectively.

To investigate element dispersion and distribution, EDS maps were obtained on polished surfaces of alkali-activated CS. As example, EDS maps of CS-GP₀-A and CS-GP_{5,0}-A are reported in Figure 22 and Figure 23, respectively. The matrix is clearly mainly composed of calcium and silicon with a lesser extent of magnesium. In particular, calcium is present in all the investigated area in both samples but some calcium

carbonate agglomerates are still recognisable as black spots in the silicon maps. Moreover, also some dolomite particles are still recognisable in both samples thanks to the presence of greener spots in the magnesium map. The presence of glass particles is evident in Figure 23 where bigger green spots are clearly visible in the silicon maps. These results confirm the formation of a calcium-silicon matrix, containing sodium and magnesium ions.

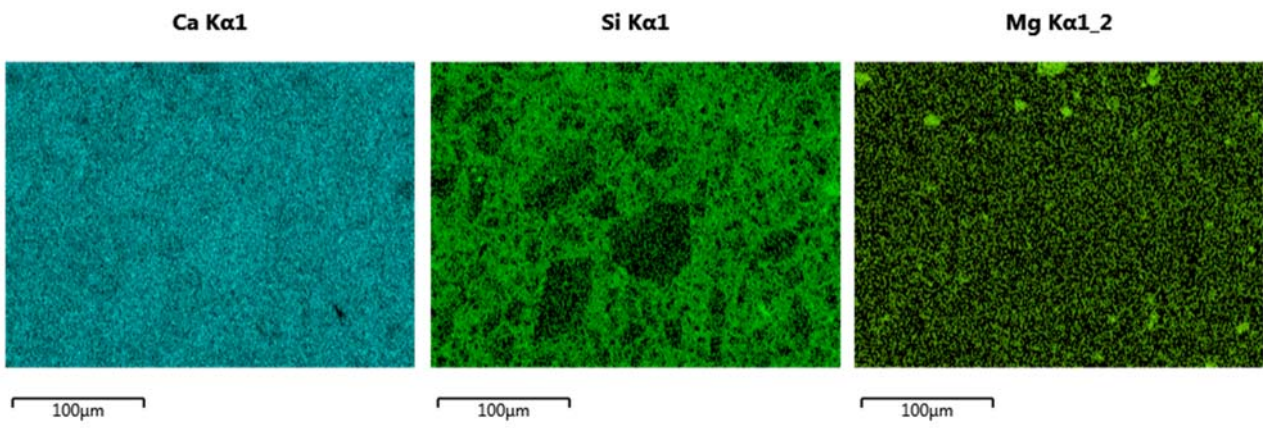


Figure 22: EDS map of CS-GP₀-A

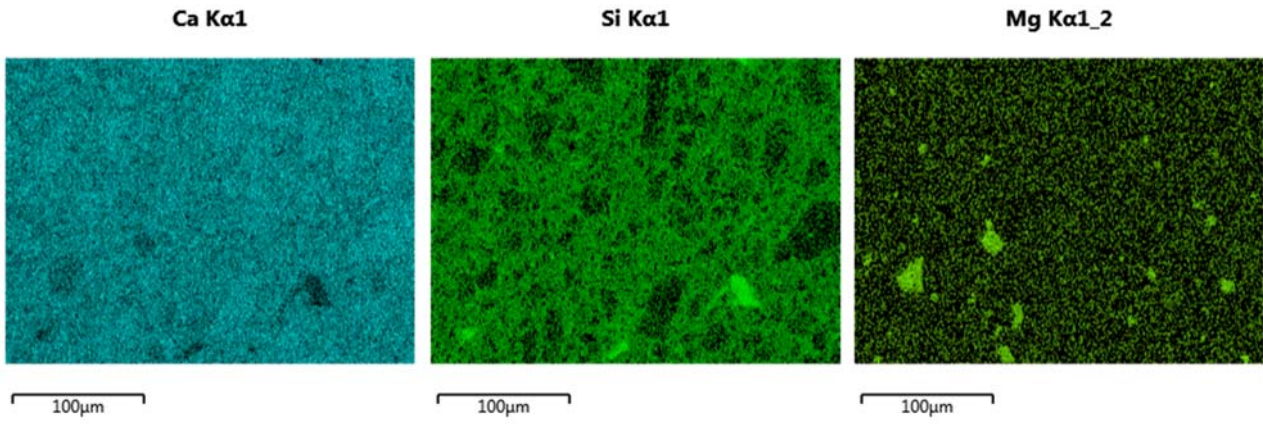


Figure 23: EDS map of CS-GP_{5.0}-A

4. Conclusions

In this paper, for the first time, alkali-activated pastes were prepared using marble sludge and waste glass powder. In particular, the influence of two glass volume percentages (2.5 and 5.0 vol%) and curing conditions (dry, humid and water immersed) were investigated. The dissolution of Ca^{2+} from calcium carbonate and its reaction with Na and Si from the activating solution to form (N)-C-S-H gel was demonstrated on the ground of several characterizations techniques and confirmed by the very high compressive strength (about 45 MPa) obtained for air-cured samples. Calcite dissolution and conversion in $\text{Ca}(\text{OH})_2$ thanks to the high pH of the activating solution promote pozzolanic reactions with the silica presents in the waterglass forming (N)-C-S-H, sodium and calcium rich silica gel and carbonates. Such compounds were initially formed in all the formulations thanks to the first day of curing in controlled conditions (i.e. 60°C and humid environment). However, after the first day, humid and water curing delay or hinder polymerisation and condensation reactions, mainly due to dissolution of specific compounds in water. Indeed, air cured samples reported the formation of a more condensed gel and a higher degree of polymerisation, as assessed by FT-IR and XPS analysis and confirmed by FE-SEM/EDX investigations. Therefore, air curing was the most favourable curing condition for mechanical properties development (compressive strengths ranging between 38 and 45 MPa after 28 days of curing were measured). Glass powder addition can provide further silica able to react with $\text{Ca}(\text{OH})_2$ improving mechanical properties thanks to pozzolanic reactions. Moreover, glass powder was effective in reducing drying shrinkage for air cured samples particularly for mixtures containing 5.0 vol% (- 70% compared to the reference sample). Finally, glass powder addition improved durability properties avoiding cracking phenomena after water immersion thanks to the higher amount of reaction products.

Acknowledgments

Authors are grateful to Best One s.r.l. for providing the carbonatic sludge, to Tecnorecuperi S.p.A. for the waste glass powder and to Ingessil s.r.l for the sodium silicate solution. Moreover, the authors wish to thank Mrs. Chiara Noé for FT-IR measurements.

References

- 1 I. Bianco, G.A. Blengini, Life Cycle Inventory of techniques for stone quarrying, cutting and finishing: Contribution to fill data gaps, *J. Clean. Prod.* 225 (2019) 684-696, <https://doi.org/10.1016/j.jclepro.2019.03.309>.
- 2 M. Traverso, G. Rizzo, M. Finkbeiner, Environmental performance of building materials: life cycle assessment of a typical Sicilian marble, *Int. J. Life Cycle Assess.* 15 (2010) 104, <https://doi.org/10.1007/s11367-009-0135-z>.
- 3 V. Liguori, G. Rizzo, M. Traverso, Marble quarrying: an energy and waste intensive activity in the production of building materials, *WIT Trans. Ecol. Envir.* 108 (2008) 197-207, <https://doi.org/10.2495/EEIA080201>.
- 4 G.M. Nicoletti, B. Notarnicola, G. Tassielli, Comparative Life Cycle Assessment of flooring materials: ceramic versus marble tiles, *J. Clean. Prod.* 10 (3) (2002) 283-296, [https://doi.org/10.1016/S0959-6526\(01\)00028-2](https://doi.org/10.1016/S0959-6526(01)00028-2).
- 5 A. Gazi, G. Skevis, M.A. Founti, Energy efficiency and environmental assessment of a typical marble quarry and processing plant, *J. Clean. Prod.* 32 (2012) 10-21, <https://doi.org/10.1016/j.jclepro.2012.03.007>.
- 6 M.E. Allam, E.S. Bakhoun, G.L. Garas, Re-use of granite sludge in producing green concrete, *J. Eng. Appl. Sci.* 9 (12) (2014) 2731-2737.
- 7 C. Furcas, G. Balletto, Converting waste from the dimension stone industry into sustainable environmental resources. Current trends, market opportunities and future outlooks, in *Proceedings of the 28th International Conference on Solid Waste Technology and Management*, University of Cagliari, Cagliari, Italy (2013).
- 8 M. Galetakis, A. Soutana, A review on the utilisation of quarry and ornamental stone industry fine by-products in the construction sector, *Constr. Build. Mater.* 102 (2016) 769-781, <https://doi.org/10.1016/j.conbuildmat.2015.10.204>.
- 9 V. Corinaldesi, G. Moriconi, T.R. Naik, Characterization of marble powder for its use in mortar and concrete, *Constr. Build. Mater.* 24 (1) (2010) 113-117, <https://doi.org/10.1016/j.conbuildmat.2009.08.013>.
- 10 A. Ergün, Effects of the usage of diatomite and waste marble powder as partial replacement of cement on the mechanical properties of concrete, *Constr. Build. Mater.* 25 (2) (2011) 806-812, <https://doi.org/10.1016/j.conbuildmat.2010.07.002>.
- 11 F. Colangelo, R. Cioffi, Use of cement kiln dust, blast furnace slag and marble sludge in the manufacture of sustainable artificial aggregates by means of cold bonding pelletization, *Materials* 6 (8) (2013) 3139-3159, <https://doi.org/10.3390/ma6083139>.
- 12 M. Bassani, L. Tefa, A. Russo, P. Palmero, Alkali-activation of recycled construction and demolition waste aggregate with no added binder, *Constr. Build. Mater.* 205 (2019) 398-413, <https://doi.org/10.1016/j.conbuildmat.2019.02.031>.
- 13 M. Bassani, L. Tefa, B. Coppola, P. Palmero, Alkali-activation of aggregate fines from construction and demolition waste: Valorisation in view of road pavement subbase applications, *J. Clean. Prod.* 234 (2019) 71-84, <https://doi.org/10.1016/j.jclepro.2019.06.207>.
- 14 L. Coppola, T. Bellezze, A. Belli, M.C. Bignozzi, F. Bolzoni, A. Brenna, et al., Binders alternative to Portland cement and waste management for sustainable construction—Part 2, *J. Appl. Biomater. Funct. Mater.* 16 (4) (2018) 207-221, <https://doi.org/10.1177%2F2280800018782852>.
- 15 B. Coppola, L. Courard, F. Michel, L. Incarnato, L. Di Maio, Investigation on the use of foamed plastic waste as natural aggregates replacement in lightweight mortar, *Compos. Part B-Eng.* 99 (2016) 75-83, <https://doi.org/10.1016/j.compositesb.2016.05.058>.
- 16 B. Coppola, L. Courard, F. Michel, L. Incarnato, P. Scarfato, L. Di Maio, Hygro-thermal and durability properties of a lightweight mortar made with foamed plastic waste aggregates, *Constr. Build. Mater.* 170 (2018) 200-206, <https://doi.org/10.1016/j.conbuildmat.2018.03.083>.

- 17 G. Ferrara, B. Coppola, L. Di Maio, L. Incarnato, E. Martinelli, Tensile strength of flax fabrics to be used as reinforcement in cement-based composites: experimental tests under different environmental exposures, *Compos. Part B-Eng.* 168 (2019) 511-523, <https://doi.org/10.1016/j.compositesb.2019.03.062>.
- 18 L. Coppola, D. Coffetti, E. Crotti, G. Gazzaniga, T. Pastore, An Empathetic Added Sustainability Index (EASI) for cementitious based construction materials, *J. Clean. Prod.* 220 (2019) 475-482, <https://doi.org/10.1016/j.jclepro.2019.02.160>.
- 19 L. Coppola, D. Coffetti, E. Crotti, T. Pastore, CSA-based Portland-free binders to manufacture sustainable concretes for jointless slabs on ground, *Constr. Build. Mater.* 187 (2018) 691-698, <https://doi.org/10.1016/j.conbuildmat.2018.07.221>.
- 20 L. Coppola, T. Bellezze, A. Belli, M.C. Bignozzi, F. Bolzoni, A. Brenna, et al., Binders alternative to Portland cement and waste management for sustainable construction–Part 1, *J. Appl. Biomater. Funct. Mater.* 16 (3) 2018 186-202, <https://doi.org/10.1177/2280800018782845>.
- 21 F. Pacheco-Torgal, J. Castro-Gomes, S. Jalali, Alkali-activated binders: A review: Part 1. Historical background, terminology, reaction mechanisms and hydration products, *Constr. Build. Mater.* 22 (7) (2008) 1305-1314, <https://doi.org/10.1016/j.conbuildmat.2007.10.015>.
- 22 J.L. Provis, Alkali-activated materials, *Cem. Concr. Res.* 114 (2018) 40-48, <https://doi.org/10.1016/j.cemconres.2017.02.009>.
- 23 P. Palmero, A. Formia, P. Antonaci, S. Brini, J.M. Tulliani, Geopolymer technology for application-oriented dense and lightened materials. Elaboration and characterization, *Ceram. Inter.* 41 (10) (2015) 12967-12979, <https://doi.org/10.1016/j.ceramint.2015.06.140>.
- 24 L. Coppola, D. Coffetti, E. Crotti, Pre-packed alkali activated cement-free mortars for repair of existing masonry buildings and concrete structures, *Constr. Build. Mater.* 173 (2018) 111-117, <https://doi.org/10.1016/j.conbuildmat.2018.04.034>.
- 25 L. Coppola, A. Buoso, D. Coffetti, P. Kara, S. Lorenzi, Electric arc furnace granulated slag for sustainable concrete, *Constr. Build. Mater.* 123 (2016) 115-119, <https://doi.org/10.1016/j.conbuildmat.2016.06.142>.
- 26 P. Palmero, A. Formia, J.M. Tulliani, P. Antonaci, Valorisation of alumino-silicate stone muds: From wastes to source materials for innovative alkali-activated materials, *Cem. Conc. Compos.* 83 (2017) 251-262, <https://doi.org/10.1016/j.cemconcomp.2017.07.011>.
- 27 L.N. Tchadjié, J.N.Y. Djobo, N. Ranjbar, H.K. Tchakouté, B.B.D. Kenne, A. Elimbi, D. Njopwouo, Potential of using granite waste as raw material for geopolymer synthesis, *Ceram. Inter.* 42 (2) (2016) 3046-3055, <https://doi.org/10.1016/j.ceramint.2015.10.091>.
- 28 M. Clausi, A.M. Fernández-Jiménez, A. Palomo, S.C. Tarantino, M. Zema, Reuse of waste sandstone sludge via alkali activation in matrices of fly ash and metakaolin, *Constr. Build. Mater.* 172 (2018) 212-223, <https://doi.org/10.1016/j.conbuildmat.2018.03.221>.
- 29 I. Tekin, Properties of NaOH activated geopolymer with marble, travertine and volcanic tuff wastes, *Constr. Build. Mater.* 127 (2016) 607-617, <https://doi.org/10.1016/j.conbuildmat.2016.10.038>.
- 30 N.K. Salihoglu, G. Salihoglu, Marble sludge recycling by using geopolymerization technology. *J. hazard. toxic radioact.* 22 (4) (2018), [https://doi.org/10.1061/\(ASCE\)HZ.2153-5515.0000415](https://doi.org/10.1061/(ASCE)HZ.2153-5515.0000415).
- 31 D.E. Ortega-Zavala, J.L. Santana-Carrillo, O. Burciaga-Díaz, J.I. Escalante-García, An initial study on alkali activated limestone binders, *Cem. Concr. Res.* 120 (2019) 267-278, <https://doi.org/10.1016/j.cemconres.2019.04.002>.
- 32 D. Ziegler, A. Formia, J. M. Tulliani, P. Palmero, Environmentally-friendly dense and porous geopolymers using fly ash and rice husk ash as raw materials, *Materials* 9 (6) (2016) 466, <https://dx.doi.org/10.3390%2Fma9060466>.
- 33 C.L. Hwang, T.P. Huynh, Effect of alkali-activator and rice husk ash content on strength development of fly ash and residual rice husk ash-based geopolymers, *Constr. Build. Mater.* 101 (2015) 1-9, <https://doi.org/10.1016/j.conbuildmat.2015.10.025>.

- 34 N. Toniolo, A.R. Boccaccini, Fly ash-based geopolymers containing added silicate waste. A review, *Ceram. Inter.* 43 (17) (2017) 14545-14551, <https://doi.org/10.1016/j.ceramint.2017.07.221>.
- 35 R.H. Geraldo, L.F. Fernandes, G. Camarini, Water treatment sludge and rice husk ash to sustainable geopolymer production, *J. Clean. Prod.* 149 (2017) 146-155, <https://doi.org/10.1016/j.jclepro.2017.02.076>.
- 36 K.T. Tong, R. Vinai, M.N. Soutsos, Use of Vietnamese rice husk ash for the production of sodium silicate as the activator for alkali-activated binders, *J. Clean. Prod.* 201 (2018) 272-286, <https://doi.org/10.1016/j.jclepro.2018.08.025>.
- 37 E. Mohseni, M.J. Kazemi, M. Koushkbaghi, B. Zehtab, B. Behforouz, Evaluation of mechanical and durability properties of fiber-reinforced lightweight geopolymer composites based on rice husk ash and nano-alumina, *Constr. Build. Mater.* 209 (2019) 532-540, <https://doi.org/10.1016/j.conbuildmat.2019.03.067>.
- 38 S.O. Sore, A. Messan, E. Prud'homme, G. Escadeillas, F. Tsobnang, Synthesis and characterization of geopolymer binders based on local materials from Burkina Faso—Metakaolin and rice husk ash, *Constr. Build. Mater.* 124 (2016) 301-311, <https://doi.org/10.1016/j.conbuildmat.2016.07.102>.
- 39 F.N. Okoye, J. Durgaprasad, N.B. Singh, Effect of silica fume on the mechanical properties of fly ash based-geopolymer concrete, *Ceram. Inter.* 42 (2) (2016) 3000-3006, <https://doi.org/10.1016/j.ceramint.2015.10.084>.
- 40 F.N. Okoye, S. Prakash, N.B. Singh, Durability of fly ash based geopolymer concrete in the presence of silica fume, *J. Clean. Prod.* 149 (2017) 1062-1067, <https://doi.org/10.1016/j.jclepro.2017.02.176>.
- 41 P. Duan, C. Yan, W. Zhou, Compressive strength and microstructure of fly ash based geopolymer blended with silica fume under thermal cycle, *Cem. Conc. Compos.* 78 (2017) 108-119, <https://doi.org/10.1016/j.cemconcomp.2017.01.009>.
- 42 Y. Wang, J. Zhao, Preliminary study on decanoic/palmitic eutectic mixture modified silica fume geopolymer-based coating for flame retardant plywood, *Constr. Build. Mater.* 189 (2018) 1-7, <https://doi.org/10.1016/j.conbuildmat.2018.08.205>.
- 43 N. Francis, B. Nakshatra, Durability of fly ash based geopolymer concrete in the presence of silica fume, *J. Clean. Prod.* 149 (2017) 1062-1067, <https://doi.org/10.1016/j.jclepro.2017.02.176>.
- 44 N.K. Lee, G.H. An, K.T. Koh, G.S. Ryu, Improved reactivity of fly ash-slag geopolymer by the addition of silica fume, *Adv. Mater. Sci. Eng.* 2016 (2016), <http://dx.doi.org/10.1155/2016/2192053>.
- 45 M. Uysal, M.M. Al-mashhadani, Y. Aygörmmez, O. Canpolat, Effect of using colemanite waste and silica fume as partial replacement on the performance of metakaolin-based geopolymer mortars, *Constr. Build. Mater.* 176 (2018) 271-282, <https://doi.org/10.1016/j.conbuildmat.2018.05.034>.
- 46 L.N. Assi, E.E. Deaver, P. Ziehl, Using sucrose for improvement of initial and final setting times of silica fume-based activating solution of fly ash geopolymer concrete, *Constr. Build. Mater.* 191 (2018) 47-55, <https://doi.org/10.1016/j.conbuildmat.2018.09.199>.
- 47 K.S. Vaibhav, M. Nagaladinni, M. Madhushree, B.P. Priya, Effect of Silica Fume on Fly Ash Based Geopolymer Mortar with Recycled Aggregates, in *Sustainable Construction and Building Materials* (2019) 595-602, Springer, Singapore, https://doi.org/10.1007/978-981-13-3317-0_52.
- 48 C. Bobirić, J.H. Shim, J.Y. Park, Leaching behavior of fly ash-waste glass and fly ash-slag-waste glass-based geopolymers, *Ceram. Inter.* 44 (6) (2018) 5886-5893, <https://doi.org/10.1016/j.ceramint.2017.12.085>.
- 49 L. Zhang, Y. Yue, Influence of waste glass powder usage on the properties of alkali-activated slag mortars based on response surface methodology, *Constr. Build. Mater.* 181 (2018) 527-534, <https://doi.org/10.1016/j.conbuildmat.2018.06.040>.
- 50 Y. Liu, C. Shi, Z. Zhang, N. Li, An overview on the reuse of waste glasses in alkali-activated materials, *Resour. Conserv. Recy.* 144 (2019) 297-309, <https://doi.org/10.1016/j.resconrec.2019.02.007>.
- 51 M. Torres-Carrasco, F. Puertas, Waste glass as a precursor in alkaline activation: Chemical process and hydration products, *Constr. Build. Mater.* 139 (2017) 342-354, <https://doi.org/10.1016/j.conbuildmat.2017.02.071>.

- 52 T. Tho-In, V. Sata, K. Boonserm, P. Chindaprasirt, Compressive strength and microstructure analysis of geopolymer paste using waste glass powder and fly ash, *J. Clean. Prod.* 172 (2018) 2892-2898, <https://doi.org/10.1016/j.jclepro.2017.11.125>.
- 53 M. Ni, B.D. Ratner, Differentiating calcium carbonate polymorphs by surface analysis techniques—an XPS and TOF-SIMS study, *Surf. Interface Anal.* 40 (10) (2008) 1356-1361, <https://doi.org/10.1002/sia.2904>.
- 54 H.W. Nesbitt, G.M. Bancroft, G.S. Henderson, R. Ho, K.N. Dalby, Y. Huang, Z. Yan, Bridging, non-bridging and free (O^{2-}) oxygen in Na_2O-SiO_2 glasses: An X-ray Photoelectron Spectroscopic (XPS) and Nuclear Magnetic Resonance (NMR) study, *J. Non-Cryst. Solids* 357(1) (2011) 170-180, <https://doi.org/10.1016/j.jnoncrsol.2010.09.031>.
- 55 M. Mastali, P. Kinnunen, A. Dalvand, R.M. Firouz, M. Illikainen, Drying shrinkage in alkali-activated binders—A critical review, *Constr. Build. Mater.* 190 (2018) 533-550, <https://doi.org/10.1016/j.conbuildmat.2018.09.125>.
- 56 F. Matalkah, T. Salem, M. Shaafaey, P. Soroushian, Drying shrinkage of alkali activated binders cured at room temperature, *Constr. Build. Mater.* 201 (2019) 563-570, <https://doi.org/10.1016/j.conbuildmat.2018.12.223>.
- 57 M. Olszak-Humienik, M. Jablonski, Thermal behavior of natural dolomite, *J. Therm. Anal. Calorim.* 119 (3) (2015) 2239-2248, <https://doi.org/10.1007/s10973-014-4301-6>.
- 58 M. Hartman, O. Trnka, V. Vesely, V. Svodoba, Thermal decomposition of the sodium carbonate hydrates, *Chem. Eng. Corn.* 185 (2001) 1-16, <https://doi.org/10.1080/00986440108912851>.
- 59 W. Ashraf, J. Olek, Carbonation activated binders from pure calcium silicates: Reaction kinetics and performance controlling factors, *Cem. Conc. Compos.* 93 (2018) 85-98, <https://doi.org/10.1016/j.cemconcomp.2018.07.004>.
- 60 A.E. Newkirk, I. Aliferis, Drying and Decomposition of Sodium Carbonate, *Anal. Chem.* 30 (5) (1958) 982-984, <https://doi.org/10.1021/ac60137a031>.
- 61 A.R. Fazeli, J.A.K. Tareen, Thermal decomposition of rhombohedral double carbonates of dolomite type, *J. Thermal Anal.* 38 (1992) 2459-65 <https://doi.org/10.1007/BF01974624>.
- 62 M.T. Wang, J.S. Cheng, M. Li, F. He, Structure and properties of soda lime silicate glass doped with rare earth, *Physica B* 406 (2) (2011) 187-191, <https://doi.org/10.1016/j.physb.2010.10.040>.
- 63 I.G. Lodeiro, D.E. Macphee, A. Palomo, A. Fernández-Jiménez, Effect of alkalis on fresh C-S-H gels. FTIR analysis, *Cem. Conc. Res.* 39 (3) (2009) 147-153, <https://doi.org/10.1016/j.cemconres.2009.01.003>.
- 64 H. Konno, Y. Nanri, M. Kitamura, Crystallization of aragonite in the causticizing reaction, *Powder Technol.* 123 (1) (2002) 33-39, [https://doi.org/10.1016/S0032-5910\(01\)00424-7](https://doi.org/10.1016/S0032-5910(01)00424-7).
- 65 A. Cwirzen, J.L. Provis, V. Penttala, K. Habermehl-Cwirzen, The effect of limestone on sodium hydroxide-activated metakaolin-based geopolymers, *Constr. Build. Mater.* 66 (2014) 53-62, <https://doi.org/10.1016/j.conbuildmat.2014.05.022>.
- 66 A. Formia, S. Terranova, P. Antonaci, N. Pugno, J. Tulliani, Setup of extruded cementitious hollow tubes as containing/releasing devices in self-healing systems, *Materials* 8 (4) (2015) 1897-1923, <https://doi.org/10.3390/ma8041897>.
- 67 H. Huang, G. Ye, Application of sodium silicate solutions as self healing agent in cementitious materials. In *Proceeding of the International Conference on Advances in Construction Materials*, Hong Kong, China, 5-7 September 2011.
- 68 U. Avila-López, J.M. Almanza-Robles, J.I. Escalante-García, Investigation of novel waste glass and limestone binders using statistical methods, *Constr. Build. Mater.* 82 (2015) 296-303, <https://doi.org/10.1016/j.conbuildmat.2015.02.085>.
- 69 J.F. Rivera, Z.I. Cuarán-Cuarán, N. Vanegas-Bonilla, R.M. de Gutiérrez, Novel use of waste glass powder: Production of geopolymeric tiles, *Adv. Powder. Technol.* 29 (12) (2018) 3448-3454, <https://doi.org/10.1016/j.appt.2018.09.023>.

- 70 N.Y. Mostafa, A.A. Shaltout, H. Omar, S.A. Abo-El-Enin, Hydrothermal synthesis and characterization of aluminium and sulfate substituted 1.1 nm tobermorites, *J. Alloys Compd.* 467 (1-2) (2009) 332-337, <https://doi.org/10.1016/j.jallcom.2007.11.130>.
- 71 P. Yu, R.J. Kirkpatrick, B. Poe, P.F. McMillan, X. Cong, Structure of calcium silicate hydrate (C-S-H): near-, mid-, and far-infrared spectroscopy, *J. Am. Ceram. Soc.* 82 (3) (1999) 742-748, <https://doi.org/10.1111/j.1151-2916.1999.tb01826.x>.
- 72 A. Sharma, H. Jain, A.C. Miller, Surface modification of a silicate glass during XPS experiments, *Surf. Interface Anal.* 31 (5) (2001) 369-374, <https://doi.org/10.1002/sia.983>.
- 73 L. Black, K. Garbev, G. Beuchle, P. Stemmermann, D. Schild, X-ray photoelectron spectroscopic investigation of nanocrystalline calcium silicate hydrates synthesised by reactive milling, *Cem. Conc. Res.* 36 (6) (2006) 1023-1031, <https://doi.org/10.1016/j.cemconres.2006.03.018>.
- 74 M.E. Simonsen, C. Sønderby, Z. Li, E.G. Sogaard, XPS and FT-IR investigation of silicate polymers, *J. Mater. Sci.* 44(8) (2009) 2079-2088, <https://doi.org/10.1007/s10853-009-3270-9>.
- 75 M. Kanuchova, L. Kozakova, M. Drabova, M. Sisol, A. Estokova, J. Kanuch, J. Skvarla, Monitoring and characterization of creation of geopolymers prepared from fly ash and metakaolin by X-ray photoelectron spectroscopy method, *Environ. Prog. Sustain.* 34 (3) (2015) 841-849, <https://doi.org/10.1002/ep.12068>.
- 76 L. Black, K. Garbev, P. Stemmermann, K.R. Hallam, G.C. Allen, X-ray photoelectron study of oxygen bonding in crystalline C-S-H phases, *Phys. Chem. Miner.* 31 (6) (2004) 337-346, <https://doi.org/10.1007/s00269-004-0401-3>.
- 77 H. Maraghechi, F. Rajabipour, C.G. Pantano, W.D. Burgos, Effect of calcium on dissolution and precipitation reactions of amorphous silica at high alkalinity, *Cem. Conc. Res.* 87 (2016) 1-13, <https://doi.org/10.1016/j.cemconres.2016.05.004>.
- 78 R. Idir, M. Cyr, A. Tagnit-Hamou, Pozzolanic properties of fine and coarse color-mixed glass cullet, *Cem. Conc. Compos.* 33(1) (2011) 19-29, <https://doi.org/10.1016/j.cemconcomp.2010.09.013>.
- 79 M. Torres-Carrasco, J. G. Palomo, F. Puertas, Sodium silicate solutions from dissolution of glasswastes. Statistical analysis, *Materiales de Construcción* 64 (314) (2014) 014, <http://dx.doi.org/10.3989/mc.2014.05213>.
- 80 S.C. Paul, B. Šavija, A.J. Babafemi, A comprehensive review on mechanical and durability properties of cement-based materials containing waste recycled glass, *J. Clean. Prod.* 198 (2018) 891-906, <https://doi.org/10.1016/j.jclepro.2018.07.095>.

Figure captions

Figure 1: XRD patterns of: a) carbonatic sludge (CS); b) glass powder (GP)

Figure 2: Particle size distribution of carbonatic sludge (CS) and glass powder (GP)

Figure 3: SEM micrographs of: a) carbonatic sludge powder (1,000× and 100,000×) and b) glass powder (1,000× and 10,000×)

Figure 4: Length variation of alkali-activated carbonatic sludge specimens: a) air-cured, b) humid cured and c) water immersed

Figure 5: Length variation of the air-cured specimens after 2, 6 and 12 days for the different glass volume fractions

Figure 6: XRD pattern of the alkali-activated carbonatic sludge after curing in different conditions (○ = Dolomite; ● = Calcite; + = Thermonatrite)

Figure 7: TGA-DTA in air of dried carbonatic sludge

Figure 8: TGA-DTA in air of the alkali-activated carbonatic sludge after curing in different conditions

Figure 9: DTG of (a) CS-GP₀-A and (b) CS-GP₀-H in the range 50-250 °C

Figure 10: FT-IR of CS and detail of the 650-950 cm⁻¹ range

Figure 11: FT-IR of glass powder and detail of the 425-1625 cm⁻¹ range

Figure 12: FT-IR of CS-GP₀ and detail of the 450-1250 cm⁻¹ range

Figure 13: Deconvolution of the Si-O vibrations band for CS-GP₀ compositions exposed at different curing conditions: a) air; b) humid and c) water

Figure 14: FT-IR of CS-GP_{2.5} and detail of the 450-1250 cm⁻¹ range

Figure 15: FT-IR of CS-GP_{5.0} and detail of the 450-1250 cm⁻¹ range

Figure 16: XPS O(1s) spectra of (a) soda-lime glass and (b) carbonatic sludge (dotted lines show the fitting results)

Figure 17: XPS O(1s) spectra of (a) CS-GP₀-A, (b) CS-GP₀-H and (c) CS-GP₀-W (dotted lines show the fitting results)

Figure 18: Flexural strength of alkali-activated carbonatic sludge after curing in different conditions for a) 14 days and b) 28 days (GP_{2.5} and GP_{5.0} means 2.5 and 5.0 vol% of glass powder)

Figure 19: Compressive strength of alkali-activated carbonatic sludge after curing in different conditions for a) 14 days and b) 28 days (GP_{2.5} and GP_{5.0} means 2.5 and 5.0 vol% of glass powder)

Figure 20: FE-SEM pictures on polished surfaces (magnification 1,000×) of alkali-activated carbonatic sludge after curing in different conditions: a) CS-GP₀-A, b) CS-GP₀-H and c) CS-GP₀-W

Figure 21: FE-SEM pictures of the pores content (magnification 50,000×) of alkali-activated carbonatic sludge after curing in different conditions: a) CS-GP₀-A, b) CS-GP₀-H and c) CS-GP₀-W

Figure 22: EDS map of CS-GP₀-A

Figure 23: EDS map of CS-GP_{5.0}-A

Tables

Table 1: XRF of the carbonatic sludge (CS) and glass powder (GP)

Table 2: Particle sizes at 10% (d_{10}), 50% (d_{50}) and 90% (d_{90}) of the cumulative distribution for CS and GP powders

Table 3: Nomenclature, composition and curing conditions (H = humid, A = air and W = water) of the alkali-activated materials